

# On Geometric Fourier Particle In Cell Methods

Martin Campos Pinto<sup>1</sup>, Jakob Ameres<sup>1,2</sup>, Katharina Kormann<sup>1,2</sup>, and Eric Sonnendrücker<sup>1,2</sup>

<sup>1</sup>Max-Planck-Institut für Plasmaphysik, Garching, Germany

<sup>2</sup>Technische Universität München, Zentrum Mathematik, Garching, Germany

February 4, 2021

## Abstract

In this article we describe a unifying framework for variational electromagnetic particle schemes of spectral type, and we propose a novel spectral Particle-In-Cell (PIC) scheme that preserves a discrete Hamiltonian structure. Our work is based on a new abstract variational derivation of particle schemes which builds on a de Rham complex where Low's Lagrangian is discretized using a particle approximation of the distribution function. In this framework, which extends the recent Finite Element based Geometric Electromagnetic PIC (GEMPIC) method to a wide variety of field solvers, the discretization of the electromagnetic potentials and fields is represented by a de Rham sequence of compatible spaces, and the particle-field coupling procedure is described by approximation operators that commute with the differential operators involved in the sequence. In particular, for spectral Maxwell solvers the choice of truncated  $L^2$  projections using continuous Fourier transform coefficients for the commuting approximation operators yields the gridless Particle-in-Fourier method, whereas spectral Particle-in-Cell methods are obtained by using discrete Fourier transform coefficients computed from a grid. By introducing a new sequence of spectral pseudo-differential approximation operators, we then obtain a novel variational spectral PIC method with discrete Hamiltonian structure that we call Fourier-GEMPIC. Fully discrete schemes are then derived using a Hamiltonian splitting procedure, leading to explicit time steps that preserve the Gauss laws and the discrete Poisson bracket associated with the Hamiltonian structure. These explicit steps are found to share many similarities with a standard spectral PIC method that appears as a Gauss and momentum-preserving variant of the variational method. As arbitrary filters are allowed in our framework, we also discuss aliasing errors and study a natural back-filtering procedure to mitigate the damping caused by anti-aliasing smoothing particle shapes.

## 1 Introduction

Representing the electromagnetic fields in truncated Fourier spaces has been a standard practice in plasma simulation, from the early particle schemes [26, 21, 3] to more recent parallel high-performance codes [37, 11, 16, 30].

In these spectral particle methods, two main approaches exist. The simplest consists of coupling the particles to the fields via continuous Fourier transforms, which leads to a gridless method sometimes called *Particle-in-Fourier* (PIF) [30, 1, 29]. This method, which may include smoothing techniques through low pass filters or smoothing shape functions, is naturally charge and energy preserving. More importantly, it can be derived from a variational principle [13, 33, 38], allowing for numerical schemes with very good stability on long time ranges. Using

the translational invariance of the discrete Fourier spaces, it has also been shown to preserve momentum.

Another approach that is often preferred for simulations where many modes are needed, such as turbulence in tokamak plasmas, is to use a grid for the coupling, and discrete Fourier transforms (DFT). This leads to spectral Particle-in-Cell (PIC) methods [24, 25, 11, 16], which we may call Fourier-PIC here. Smooth (continuous) particle shapes are then necessary for the coupling to be well-defined, which in Fourier space corresponds to a low-pass filtering. Using a DFT grid allows to localize the coupling, but it also causes dispersion and aliasing errors [24, 25, 3], which in turn have been shown to lead to numerical instabilities of various types, including grid heating [4], electrostatic finite grid instabilities [22] and numerical Cherenkov instabilities [15, 40, 16]. In most cases these methods are momentum preserving and in some cases they are also charge preserving, see e.g. [16]. However, it seems that until very recently a proper derivation of variational spectral PIC methods was still missing.

This has been done in part in a new article [9] where a flexible yet rigorous method is proposed to design variational, gauge-free electromagnetic particle schemes with a Hamiltonian structure relying on a non-canonical discrete Poisson bracket. Formulated in a general framework with a minimal set of properties, this approach essentially extends the recent Geometric Electromagnetic PIC (GEMPIC) scheme [23], based on spline finite elements and point particles, to a wide range of field solvers and particle coupling techniques. In particular, one application described in [9] consists of a new Hamiltonian spectral PIC method, where the particle-field coupling is done through a DFT grid. However, as this method relies on particle-field operators defined through geometric degrees of freedom, the resulting deposition algorithms involve volume integrals of the shaped particles as they travel through space, which somehow deviates from standard PIC scheme that are based on pointwise evaluations of the particle shape functions.

In this article we thus propose a novel variational spectral PIC method called Fourier-Gempic, that has a discrete Hamiltonian structure and relies on particle-field coupling techniques very similar to those encountered in standard PIC schemes. Our method is obtained by applying the abstract derivation of [9] to truncated Fourier spaces, combined with novel particle-field coupling operators of pseudo-differential type. By observing that our variational derivation combined with continuous ( $L^2$ -orthogonal) projection operators leads to the grid-less PIF method, we show that this framework actually unifies the formulation of variational spectral particle methods, where the standard PIC scheme appears as a momentum-conserving variant, albeit non-variational.

By applying a Hamiltonian splitting technique in the spirit of [10, 19] we are able to propose fully discrete schemes for the three different methods, with explicit time steps that provide an additional insight into their differences and similarities. For the Hamiltonian GEMPIF and Fourier-GEMPIC methods, these fully discrete schemes preserve the total energy within the time splitting error as guaranteed by backward error analysis [17]. For the PIF and standard PIC methods, they preserve the total momentum. All of them preserve the Gauss laws to machine accuracy.

In addition to a Hamiltonian structure which guarantees very good stability properties on long time ranges, the Fourier-Gempic method has the ability to include various shape functions and filter coefficients in Fourier space. In particular, we show that a natural back-filtering mechanism can be associated to the usual low-pass filtering effect of high order spline shapes in order to strongly reduce aliasing errors inherent in the DFT, without damping relevant modes in the computational range.

The outline is as follows. In Section 2 we recall the two main coupling approaches for Fourier-

particle methods, namely Particle-in-Fourier (PIF) and Fourier-PIC, we discuss aliasing errors and consider a simple back-filtering technique to mitigate the smoothing effect of anti-aliasing splines. In Section 3 we then present the general form of a variational spectral scheme as derived in [9], as well as that of the momentum-conserving variant, and apply it to two particular sets of particle-field approximation operators: using  $L^2$  projections which correspond to continuous Fourier coefficients, this leads to the gridless PIF method, which coincides with its momentum-conserving variant. Using a novel class of pseudo-differential DFT operators, we obtain a new Fourier-PIC method, whose Hamiltonian structure is guaranteed by the commuting de Rham diagram property of the new DFT approximation operators and the analysis from [9]. In Section 4 we then describe fully discrete schemes of arbitrary orders, obtained by applying a Hamiltonian splitting procedure. Both in the gridless and PIC cases, we provide explicit formulas for the different steps of the discrete schemes. The standard Fourier-PIC coupling is then found to coincide with the momentum-conserving variant of the Hamiltonian Fourier-GEMPIC method, while the latter differs in the computation of the pushing fields. In Section 5 we assess the basic numerical properties of the different methods. Their accuracy is compared on standard test cases, as well as their long-time stability and conservation properties. It is shown that all Hamiltonian methods are very stable in energy and momentum, and that back-filtered methods are very accurate for approximating the fundamental growth and damping rates, even for low-resolution runs.

## 2 Spectral particle methods, with or without a grid

Electromagnetic particle models formally consist of Maxwell's equations for the fields,

$$\partial_t \mathbf{E}(\mathbf{x}, t) - \text{curl } \mathbf{B}(\mathbf{x}, t) = -\mathbf{J}_N(\mathbf{x}, t) \quad (1)$$

$$\partial_t \mathbf{B}(\mathbf{x}, t) + \text{curl } \mathbf{E}(\mathbf{x}, t) = 0 \quad (2)$$

$$\text{div } \mathbf{E}(\mathbf{x}, t) = \rho_N(\mathbf{x}, t) \quad (3)$$

$$\text{div } \mathbf{B}(\mathbf{x}, t) = 0, \quad (4)$$

coupled with discrete particles with positions  $\mathbf{X}_p$  and velocities  $\mathbf{V}_p$ ,  $p = 1, \dots, N$ , subject to Lorentz force trajectories

$$\frac{d}{dt} \mathbf{X}_p(t) = \mathbf{V}_p(t), \quad \frac{d}{dt} \mathbf{V}_p(t) = \frac{q_p}{m_p} (\mathbf{E}(\mathbf{X}_p(t), t) + \mathbf{V}_p(t) \times \mathbf{B}(\mathbf{X}_p(t), t)). \quad (5)$$

Here  $q_p$  and  $m_p$  represent the charge and mass of the  $p$ -th numerical particle, and the current and charge densities, which are the sources in Maxwell's equations, are obtained by summing each particle contribution,

$$\rho_N(t, \mathbf{x}) = \sum_{p=1 \dots N} q_p \delta(\mathbf{x} - \mathbf{X}_p(t)) \quad \text{and} \quad \mathbf{J}_N(t, \mathbf{x}) = \sum_{p=1 \dots N} q_p \mathbf{V}_p(t) \delta(\mathbf{x} - \mathbf{X}_p(t)). \quad (6)$$

In the limit  $N \rightarrow \infty$  of infinitely many particles, this model approximates the kinetic Vlasov equation [36] where the plasma is represented by a continuous phase-space density function  $f(t, \mathbf{x}, \mathbf{v})$ , and the choice of Dirac densities in (6) corresponds to a pointwise evaluation of the continuous charge and current densities  $\rho(t, \mathbf{x}) = \int q f(t, \mathbf{x}, \mathbf{v}) d\mathbf{v}$ ,  $\mathbf{J}(t, \mathbf{x}) = \int q \mathbf{v} f(t, \mathbf{x}, \mathbf{v}) d\mathbf{v}$ .

In spectral solvers, electromagnetic fields are represented by truncated Fourier expansions

of the form

$$\begin{cases} \mathbf{E}_K(t, \mathbf{x}) = \sum_{\mathbf{k} \in \llbracket -K, K \rrbracket^3} \mathbf{E}_{\mathbf{k}}(t) e^{\frac{2i\pi \mathbf{k} \cdot \mathbf{x}}{L}} \\ \mathbf{B}_K(t, \mathbf{x}) = \sum_{\mathbf{k} \in \llbracket -K, K \rrbracket^3} \mathbf{B}_{\mathbf{k}}(t) e^{\frac{2i\pi \mathbf{k} \cdot \mathbf{x}}{L}} \end{cases} \quad \text{for } \mathbf{x} \in [0, L]^3, \quad (7)$$

here with  $2K + 1$  modes per dimension, and the sources need to be properly represented in the same truncated Fourier spaces. The discrete Maxwell's equations then take the form

$$\begin{cases} -\partial_t \mathbf{E}_{\mathbf{k}} + \left( \frac{2i\pi \mathbf{k}}{L} \right) \times \mathbf{B}_{\mathbf{k}} = \mathbf{J}_{\mathbf{k}}^S, \\ \partial_t \mathbf{B}_{\mathbf{k}} + \left( \frac{2i\pi \mathbf{k}}{L} \right) \times \mathbf{E}_{\mathbf{k}} = 0 \end{cases} \quad \text{for } \mathbf{k} \in \llbracket -K, K \rrbracket^3 \quad (8)$$

and the trajectory equations for the particles read

$$\begin{cases} \frac{d}{dt} \mathbf{X}_p = \mathbf{V}_p, \\ \frac{d}{dt} \mathbf{V}_p = \frac{q_p}{m_p} (\mathbf{E}^S(\mathbf{X}_p) + \mathbf{V}_p \times \mathbf{B}^S(\mathbf{X}_p)) \end{cases} \quad \text{for } p \in \llbracket 1, N \rrbracket. \quad (9)$$

In (8)–(9) we have denoted the coupling terms by

- $\mathbf{J}_{\mathbf{k}}^S$  the Fourier coefficients of the current density seen by the discrete field,
- $\mathbf{E}^S$  and  $\mathbf{B}^S$ , the electromagnetic field seen by the particles.

These coupling terms involve a shape function  $S$  which is primarily used to define an auxiliary particle current density

$$\mathbf{J}_N^S(\mathbf{x}) := \mathbf{J}_N * S(\mathbf{x}) = \sum_{p=1}^N q_p \mathbf{V}_p S(\mathbf{x} - \mathbf{X}_p) \quad (10)$$

from which the Fourier coefficients  $\mathbf{J}_{\mathbf{k}}^S$  are derived. This shape  $S$  may either be the Dirac mass or some smooth approximation of it such as a B-spline, in which case  $\mathbf{J}_N^S$  corresponds to a convolution smoothing of  $\mathbf{J}_N = \mathbf{J}_N^\delta$ .

How the coupling terms are precisely defined will then characterize the numerical method at this semi-discrete level. Spectral particle methods can essentially be divided in two classes: gridless *Particle-in-Fourier* methods where the particles are directly coupled to the fields, and *Particle-in-Cell* methods that use an intermediate grid and a Discrete Fourier Transform (DFT) to localize the coupling steps. In the remainder of this section we recall the main features of these methods and discuss aliasing errors and anti-aliasing techniques.

## 2.1 Gridless coupling: the Particle-In-Fourier (PIF) approach

The simplest option consists of a gridless coupling as in e.g. [26, 37, 11, 13], which leads to a method sometimes called *Particle-in-Fourier* [30, 1, 29]. Here, the coupling current terms  $\mathbf{J}_{\mathbf{k}}^S$  are simply obtained as the Fourier coefficients of  $\mathbf{J}_N^S$ . Letting

$$\mathcal{F}_{\mathbf{k}}(G) := \left( \frac{1}{L} \right)^3 \int_{[0, L]^3} G(\mathbf{x}) e^{-\frac{2i\pi \mathbf{k} \cdot \mathbf{x}}{L}} d\mathbf{x} \quad (11)$$

denote the  $\mathbf{k}$ -th (continuous) Fourier coefficient of an arbitrary function  $G$ , this gives

$$\mathbf{J}_{\mathbf{k}}^S := \mathcal{F}_{\mathbf{k}}(\mathbf{J}_N^S) = \left(\frac{1}{L}\right)^3 \sum_{p=1 \dots N} q_p \mathbf{V}_p \int_{[0,L]^3} S(\mathbf{x} - \mathbf{X}_p) e^{-\frac{2i\pi \mathbf{k} \cdot \mathbf{x}}{L}} d\mathbf{x}. \quad (12)$$

The coupling fields are then defined by continuous convolution products

$$\mathbf{E}^S(\mathbf{x}) = \int_{[0,L]^3} \mathbf{E}_K(\tilde{\mathbf{x}}) S(\tilde{\mathbf{x}} - \mathbf{x}) d\tilde{\mathbf{x}}, \quad \mathbf{B}^S(\mathbf{x}) = \int_{[0,L]^3} \mathbf{B}_K(\tilde{\mathbf{x}}) S(\tilde{\mathbf{x}} - \mathbf{x}) d\tilde{\mathbf{x}} \quad (13)$$

evaluated at the particle positions  $\mathbf{x} = \mathbf{X}_p$ . It will sometimes be convenient to rewrite this gridless coupling in terms of the Fourier coefficients of the function  $S_{\mathbf{X}_p}(\mathbf{x}) = S(\mathbf{x} - \mathbf{X}_p)$ , as

$$\mathbf{J}_{\mathbf{k}}^S = \sum_{p=1 \dots N} q_p \mathbf{V}_p \mathcal{F}_{\mathbf{k}}(S_{\mathbf{X}_p}) \quad (14)$$

and

$$\mathbf{E}^S(\mathbf{X}_p) = L^3 \sum_{\mathbf{k} \in \llbracket -K, K \rrbracket^3} \mathbf{E}_{\mathbf{k}} \overline{\mathcal{F}_{\mathbf{k}}(S_{\mathbf{X}_p})}, \quad \mathbf{B}^S(\mathbf{X}_p) = L^3 \sum_{\mathbf{k} \in \llbracket -K, K \rrbracket^3} \mathbf{B}_{\mathbf{k}} \overline{\mathcal{F}_{\mathbf{k}}(S_{\mathbf{X}_p})}, \quad (15)$$

where  $\overline{\mathcal{F}}$  denotes the complex conjugate of  $\mathcal{F}$ . We note that here a Dirac shape can be used,  $S = \delta$ , since Fourier coefficients are well defined for Dirac distributions [14],

$$\mathcal{F}_{\mathbf{k}}(\delta_{\mathbf{X}_p}) = \left(\frac{1}{L}\right)^3 e^{-\frac{2i\pi \mathbf{k} \cdot \mathbf{X}_p}{L}}$$

and this is indeed a standard option in gridless methods [30, 1]. Here we keep the possibility of using arbitrary shapes, for the sake of generality and clarity of exposition.

In [13, 33] it was shown that this semi-discrete system can be derived from a discrete variational principle, and that it preserves exactly the charge (namely the Gauss laws), as well as the total energy and momentum of the system. However, the coupling is global: every particle contributes directly to every Fourier mode, and vice versa. For problems involving a large number of Fourier modes, this leads to a computational complexity of  $\mathcal{O}(NK^3)$  which is prohibitive for simulations using a large number  $N$  of particles.

## 2.2 Coupling with a DFT grid: the spectral or Fourier-PIC approach

A standard approach [24, 25, 21, 3] consists of using an intermediate grid with  $M$  points per dimension,  $M \geq 2K + 1$ , and discrete Fourier transforms (DFT), which is more efficient for simulations where a large number of Fourier modes are needed. This approach is sometimes referred to as spectral or pseudo-spectral PIC [11, 16]. Denoting by

$$\mathcal{F}_{M,\mathbf{k}}(G) := \left(\frac{1}{M}\right)^3 \sum_{\mathbf{m} \in \llbracket 1, M \rrbracket^3} G(\mathbf{m}h) e^{-\frac{2i\pi \mathbf{k} \cdot \mathbf{m}}{M}} \quad \text{with} \quad h = \frac{L}{M}, \quad (16)$$

the *discrete* Fourier coefficients associated with this grid, the current source is then defined as

$$\mathbf{J}_{\mathbf{k}}^S := \mathcal{F}_{M,\mathbf{k}}(\mathbf{J}_N^S) \quad (17)$$

with a smoothed current density given again by  $\mathbf{J}_N^S = \mathbf{J}_N * S$ , see (10). In practice this amounts to first depositing this current on the grid as in a standard Particle-in-Cell method,

$$\mathbf{J}_{\mathbf{m}}^{\text{pic}} := \mathbf{J}_N^S(\mathbf{m}h) = \sum_{p=1 \dots N} q_p \mathbf{V}_p S(\mathbf{m}h - \mathbf{X}_p) \quad \text{for} \quad \mathbf{m} \in \llbracket 1, M \rrbracket^3$$

and then performing a DFT,

$$\mathbf{J}_k^S = \left(\frac{1}{M}\right)^3 \sum_{\mathbf{m} \in \llbracket 1, M \rrbracket^3} \mathbf{J}_m^{\text{pic}} e^{-\frac{2i\pi \mathbf{k} \cdot \mathbf{m}}{M}} \quad \text{for } \mathbf{k} \in \llbracket -K, K \rrbracket^3.$$

The pushing fields are then defined by a discrete convolution,

$$\mathbf{E}^S(\mathbf{x}) := h^3 \sum_{\mathbf{m} \in \llbracket 1, M \rrbracket^3} \mathbf{E}_K(\mathbf{m}h) S(\mathbf{m}h - \mathbf{x}), \quad \mathbf{B}^S(\mathbf{x}) := h^3 \sum_{\mathbf{m} \in \llbracket 1, M \rrbracket^3} \mathbf{B}_K(\mathbf{m}h) S(\mathbf{m}h - \mathbf{x}) \quad (18)$$

also evaluated at the particle positions  $\mathbf{x} = \mathbf{X}_p$ . In practice the steps are similar, in a transposed order: the field values (7) are first computed on the grid, which corresponds to an inverse DFT

$$\begin{cases} \mathbf{E}_m^{\text{pic}} := \mathbf{E}_K(\mathbf{m}h) = \sum_{\mathbf{k} \in \llbracket -K, K \rrbracket^3} \mathbf{E}_k e^{\frac{2i\pi \mathbf{k} \cdot \mathbf{m}}{M}} \\ \mathbf{B}_m^{\text{pic}} := \mathbf{B}_K(\mathbf{m}h) = \sum_{\mathbf{k} \in \llbracket -K, K \rrbracket^3} \mathbf{B}_k e^{\frac{2i\pi \mathbf{k} \cdot \mathbf{m}}{M}} \end{cases} \quad \text{for } \mathbf{m} \in \llbracket 1, M \rrbracket^3,$$

and they are gathered on the particles with the shape function  $S$ , as in a standard PIC method

$$\begin{cases} \mathbf{E}^S(\mathbf{X}_p) = h^3 \sum_{\mathbf{m} \in \llbracket 1, M \rrbracket^3} \mathbf{E}_m^{\text{pic}} S(\mathbf{m}h - \mathbf{X}_p) \\ \mathbf{B}^S(\mathbf{X}_p) = h^3 \sum_{\mathbf{m} \in \llbracket 1, M \rrbracket^3} \mathbf{B}_m^{\text{pic}} S(\mathbf{m}h - \mathbf{X}_p). \end{cases}$$

We note that these coupling terms can be rewritten in a form similar to (14)–(15), now with the discrete Fourier coefficients of the function  $S_{\mathbf{X}_p}(\mathbf{x}) = S(\mathbf{x} - \mathbf{X}_p)$ . Indeed we have

$$\mathbf{J}_k^S = \sum_{p=1 \dots N} q_p \mathbf{V}_p \mathcal{F}_{M, \mathbf{k}}(S_{\mathbf{X}_p}) \quad (19)$$

and

$$\mathbf{E}^S(\mathbf{X}_p) = L^3 \sum_{\mathbf{k} \in \llbracket -K, K \rrbracket^3} \mathbf{E}_k \overline{\mathcal{F}_{M, \mathbf{k}}(S_{\mathbf{X}_p})}, \quad \mathbf{B}^S(\mathbf{X}_p) = L^3 \sum_{\mathbf{k} \in \llbracket -K, K \rrbracket^3} \mathbf{B}_k \overline{\mathcal{F}_{M, \mathbf{k}}(S_{\mathbf{X}_p})}. \quad (20)$$

For these terms to be well-defined, we see that  $S$  must now be at least continuous. A common choice is to take (the periodic extension of) a tensor-product B-spline of degree  $\kappa \geq 1$  scaled to the grid,

$$S(\mathbf{x}) := \sum_{\mathbf{r} \in \mathbb{Z}^3} S_\kappa^h(\mathbf{x} + \mathbf{r}L) \quad \text{where} \quad S_\kappa^h(\mathbf{x}) := \left(\frac{1}{h}\right)^3 \prod_{\alpha \in \llbracket 1, 3 \rrbracket} \hat{S}_\kappa\left(\frac{x_\alpha}{h}\right), \quad (21)$$

with cardinal univariate B-splines defined on the reference grid as  $\hat{S}_0(x) := \mathbb{1}_{[-\frac{1}{2}, \frac{1}{2}]}(x)$  and

$$\hat{S}_\kappa(x) := \hat{S}_0 * \hat{S}_{\kappa-1}(x) = \int_{-\frac{1}{2}}^{\frac{1}{2}} \hat{S}_{\kappa-1}(x-y) dy \quad \text{for } \kappa \geq 1.$$

As these shape functions have localized supports,  $\text{supp}(S) = [-h(\frac{\kappa+1}{2}), h(\frac{\kappa+1}{2})]$ , the particles only interact with the  $(\kappa+1)^3$  neighbouring grid nodes, which makes the deposition/gathering

steps local. Moreover if  $M$  is a power of two, then the DFTs can be efficiently performed with an FFT algorithm, leading to a computational complexity of  $\mathcal{O}(N(\kappa + 1)^3) + \mathcal{O}(M^3 \log(M))$  that is more affordable in simulations involving a large number of particles and Fourier modes. In [29] it is observed that combining DFT couplings with the filtering method of [34] provides an efficient approximation of the gridless method, corresponding to a *nonequispaced fast Fourier transform* [32]. This technique will be revisited in Section 2.4 as a natural back-filtering method. More generally, we note that Fourier filtering is commonly used in modern PIC codes in order to reduce the statistical noise inherent to particle approximations, see e.g. [28, 18].

Fourier-PIC coupling often leads to momentum-preserving schemes. In some cases they have been shown to be also charge-preserving, see e.g. [16] where the DFT current deposition is seen as a spectral adaptation of the classical Esirkepov method [12]. However, it does not preserve the energy and in general it cannot be derived from a variational principle.

### 2.3 Shape filtering and grid aliasing in Fourier space

As is well known (see e.g. [3, Sec. 8-7]), smooth particle shapes have a low-pass filtering effect in Fourier space. This is most easily seen in the gridless case, where the coupling fields (12)–(13) defined by continuous convolution products satisfy

$$\mathbf{J}_{\mathbf{k}}^S = \sigma_{\mathbf{k}} \mathcal{F}_{\mathbf{k}}(\mathbf{J}_N) \quad \text{for } \mathbf{k} \in \llbracket -K, K \rrbracket^3 \quad (22)$$

and

$$\begin{cases} \mathcal{F}_{\mathbf{k}}(\mathbf{E}^S) = \overline{\sigma_{\mathbf{k}}} \mathbf{E}_{\mathbf{k}} \\ \mathcal{F}_{\mathbf{k}}(\mathbf{B}^S) = \overline{\sigma_{\mathbf{k}}} \mathbf{B}_{\mathbf{k}} \end{cases} \quad \text{for } \mathbf{k} \in \mathbb{Z}^3 \quad (23)$$

where we have denoted  $\sigma_{\mathbf{k}} := L^3 \mathcal{F}_{\mathbf{k}}(S)$  and set  $\mathbf{E}_{\mathbf{k}} := \mathbf{B}_{\mathbf{k}} := 0$  for  $|\mathbf{k}|_{\infty} > K$ . Notice that  $\overline{\sigma_{\mathbf{k}}} = \sigma_{\mathbf{k}}$  for symmetric shapes. As smoother functions are associated with faster decreasing spectra, we can clearly see the filtering effect of smooth shapes. Specifically, with the Dirac shape  $S = \delta$  we have  $\sigma_{\mathbf{k}} = 1$  for all  $\mathbf{k}$ , hence no filtering. With a B-spline (21) of degree  $\kappa \in \mathbb{N}$  and scale  $h = L/M$ , we have

$$\sigma_{\mathbf{k}} = L^3 \mathcal{F}_{\mathbf{k}}(S) = \prod_{\alpha=1}^3 \left( \text{sinc} \left( \frac{\pi k_{\alpha}}{\mu(2K+1)} \right) \right)^{\kappa+1} \quad \text{with} \quad \mu := \frac{M}{2K+1} \geq 1. \quad (24)$$

Here  $\text{sinc}(\theta) := \frac{1}{\theta} \sin \theta$  and  $\mu$  is the *oversampling parameter*. Since  $|\frac{\pi k_{\alpha}}{\mu(2K+1)}| < \frac{\pi}{2\mu} \leq \frac{\pi}{2}$  for  $\mathbf{k} \in \llbracket -K, K \rrbracket^3$ , this makes explicit how modes  $|\mathbf{k}|_{\infty} \approx K$  are damped with “smoother” splines, namely higher degrees and coarser grids.

In the Fourier-PIC case a similar filtering effect can be observed, but an additional phenomenon enters into play. Indeed the use of a grid leads to the well-known *aliasing* effect [5], an  $M$ -periodization of the discrete Fourier coefficients through the superposition of high frequency modes, i.e.

$$\mathcal{F}_{M,\mathbf{k}}(G) = \sum_{\ell \in \mathbb{Z}^3} \mathcal{F}_{\mathbf{k}+\ell M}(G) \quad \text{for any } G \in \mathcal{C}_{\text{per}}^0.$$

Applying this equality to  $\mathbf{J}_N^S$  and using again that  $\mathcal{F}_{\mathbf{k}}(\mathbf{J}_N^S) = \sigma_{\mathbf{k}} \mathcal{F}_{\mathbf{k}}(\mathbf{J}_N)$ , we find that in the Fourier-PIC case the modes of the coupling current (17) read

$$\mathbf{J}_{\mathbf{k}}^S = \sum_{\ell \in \mathbb{Z}^3} \sigma_{\mathbf{k}+\ell M} \mathcal{F}_{\mathbf{k}+\ell M}(\mathbf{J}_N) \quad \text{for } \mathbf{k} \in \llbracket -K, K \rrbracket^3. \quad (25)$$

Here the aliases are the modes corresponding to  $\ell \neq 0$ , all outside the main range  $\llbracket -K, K \rrbracket^3$ , since  $M \geq 2K + 1$ . For the pushing fields (18) the discrete convolution leads to a dual aliasing phenomenon, of the form

$$\begin{cases} \mathcal{F}_{\mathbf{k}}(\mathbf{E}^S) = \overline{\sigma_{\mathbf{k}}} \sum_{\ell \in \mathbb{Z}^3} \mathbf{E}_{\mathbf{k} + \ell M} \\ \mathcal{F}_{\mathbf{k}}(\mathbf{B}^S) = \overline{\sigma_{\mathbf{k}}} \sum_{\ell \in \mathbb{Z}^3} \mathbf{B}_{\mathbf{k} + \ell M} \end{cases} \quad \text{for } \mathbf{k} \in \mathbb{Z}^3. \quad (26)$$

Again, the aliases consist of the  $\ell \neq 0$  terms, which now correspond to the main modes of  $\mathbf{E}_K$  and  $\mathbf{B}_K$  contributing to *higher* frequencies of the coupling field. Indeed, using that  $\mathbf{E}_{\mathbf{k}} = 0$  for  $\mathbf{k} \notin \llbracket -K, K \rrbracket^3$  we may rewrite (26) as

$$\mathcal{F}_{\mathbf{k}'}(\mathbf{E}^S) = \begin{cases} \overline{\sigma_{\mathbf{k} + \ell M}} \mathbf{E}_{\mathbf{k}} & \text{for } \mathbf{k}' = \mathbf{k} + \ell M \in \llbracket -K, K \rrbracket^3 + M\mathbb{Z}^3 \\ 0 & \text{for } \mathbf{k}' \notin \llbracket -K, K \rrbracket^3 + M\mathbb{Z}^3 \end{cases} \quad (27)$$

and similarly for  $\mathbf{B}^S$ .

The repercussions of aliasing in numerical simulations have been studied since the early days of computational plasma modelling, either through linearized dispersion analysis or fully nonlinear studies [24, 31, 15, 25]. By introducing spurious modes which can then be coupled in the nonlinear models, aliasing has often been recognized as the source of many issues in the simulations, including grid heating [4], finite grid instabilities [22] and numerical Cherenkov instabilities [40, 16].

## 2.4 Anti-aliasing and back-filtering

It is clear from (25)–(27) that smooth shapes with a low-pass filtering effect, such as B-splines, may be used for anti-aliasing purposes. However, by filtering also some frequencies within the computational range  $\llbracket -K, K \rrbracket^3$ , they can lead to the *overdamping* of relevant modes, in particular for low-resolution discretizations.

In order to mitigate the aliasing errors and thus reduce the associated instabilities, a successful approach has consisted in associating the anti-aliasing properties of smooth spline shapes with additional ad-hoc filters. In [16] for instance, the authors show that many instabilities can be strongly reduced by using filters determined so as to reduce specific growing modes in the dispersion relations. And in [29], the particular DFT coupling that is proposed to reduce aliasing is based on the nonequispaced fast Fourier transforms (NFFT) [34, 32] which precisely involves filter coefficients that match the low-pass filter effect of the smoothing splines.

Here we propose to interpret these filtering techniques as an effective *back-filtering* method. Indeed, it is easily seen from (25) that a simple solution for the overdamping issue consists of dividing each deposited current mode with the corresponding shape filter coefficient, leading to a new current defined as

$$\mathbf{J}_{\mathbf{k}}^{S,\text{bf}} := \frac{1}{\sigma_{\mathbf{k}}} \mathcal{F}_{M,\mathbf{k}}(\mathbf{J}_N^S). \quad (28)$$

For the pushing fields the idea is the same but we see from (26) that the back-filtering needs to be applied on the original field, rather than on the coupling terms. This leads to setting

$$\mathbf{E}^{S,\text{bf}}(\mathbf{x}) := h^3 \sum_{\mathbf{m} \in \llbracket 1, M \rrbracket^3} \mathbf{E}_K^{\text{bf}}(\mathbf{m}h) S(\mathbf{m}h - \mathbf{x}), \quad \mathbf{B}^{S,\text{bf}}(\mathbf{x}) := h^3 \sum_{\mathbf{m} \in \llbracket 1, M \rrbracket^3} \mathbf{B}_K^{\text{bf}}(\mathbf{m}h) S(\mathbf{m}h - \mathbf{x}) \quad (29)$$



with back-filtered fields defined as

$$\begin{cases} \mathbf{E}_K^{\text{bf}}(\mathbf{x}) := \sum_{\mathbf{k} \in \llbracket -K, K \rrbracket^3} \overline{\left(\frac{1}{\sigma_{\mathbf{k}}}\right)} \mathbf{E}_{\mathbf{k}} e^{\frac{2i\pi \mathbf{k} \cdot \mathbf{x}}{L}} \\ \mathbf{B}_K^{\text{bf}}(\mathbf{x}) := \sum_{\mathbf{k} \in \llbracket -K, K \rrbracket^3} \overline{\left(\frac{1}{\sigma_{\mathbf{k}}}\right)} \mathbf{B}_{\mathbf{k}} e^{\frac{2i\pi \mathbf{k} \cdot \mathbf{x}}{L}}. \end{cases} \quad (30)$$

With this coupling, formulas (25)–(26) become

$$\mathbf{J}_{\mathbf{k}}^{S,\text{bf}} = \mathcal{F}_{\mathbf{k}}(\mathbf{J}_N) + \sum_{\ell \neq 0} \frac{\sigma_{\mathbf{k}+\ell M}}{\sigma_{\mathbf{k}}} \mathcal{F}_{\mathbf{k}+\ell M}(\mathbf{J}_N) \quad \text{for } \mathbf{k} \in \llbracket -K, K \rrbracket^3 \quad (31)$$

and

$$\begin{cases} \mathcal{F}_{\mathbf{k}}(\mathbf{E}^{S,\text{bf}}) = \mathbf{E}_{\mathbf{k}} + \sum_{\ell \neq 0} \overline{\left(\frac{\sigma_{\mathbf{k}}}{\sigma_{\mathbf{k}+\ell M}}\right)} \mathbf{E}_{\mathbf{k}+\ell M} \\ \mathcal{F}_{\mathbf{k}}(\mathbf{B}^{S,\text{bf}}) = \mathbf{B}_{\mathbf{k}} + \sum_{\ell \neq 0} \overline{\left(\frac{\sigma_{\mathbf{k}}}{\sigma_{\mathbf{k}+\ell M}}\right)} \mathbf{B}_{\mathbf{k}+\ell M} \end{cases} \quad \text{for } \mathbf{k} \in \mathbb{Z}^3 \quad (32)$$

where we have separated each contribution into its main mode ( $\ell = 0$ ) and the filtered aliases. And again, using explicitly that  $\mathbf{E}_{\mathbf{k}} = 0$  for  $\mathbf{k} \notin \llbracket -K, K \rrbracket^3$  we can rewrite (32) as

$$\mathcal{F}_{\mathbf{k}'}(\mathbf{E}^{S,\text{bf}}) = \begin{cases} \overline{\left(\frac{\sigma_{\mathbf{k}+\ell M}}{\sigma_{\mathbf{k}}}\right)} \mathbf{E}_{\mathbf{k}} & \text{if } \mathbf{k}' = \mathbf{k} + \ell M \in \llbracket -K, K \rrbracket^3 + M\mathbb{Z}^3 \\ 0 & \text{if } \mathbf{k}' \notin \llbracket -K, K \rrbracket^3 + M\mathbb{Z}^3 \end{cases} \quad (33)$$

and similarly for  $\mathbf{B}^{S,\text{bf}}$ . For B-splines we can see from (24) that  $\sigma_{\mathbf{k}}$  is far from 0 in the range  $\mathbf{k} \in \llbracket -K, K \rrbracket^3$ . Thus, back-filtering allows to reduce the amplitude of all the aliased modes in a similar proportion as with a standard filtering, but without damping any mode in the computational range.

### 3 Variational spectral particle discretizations

In this section we follow the variational structure-preserving discretization framework of [9] and apply it to discrete Fourier spaces. This essentially allows us to extend the Finite Element spline GEMPIC method from [23] to spectral Maxwell solvers.

#### 3.1 Structure-preserving particle-field discretizations

We remind that a central feature of this framework is to preserve the de Rham sequence of  $\mathbb{R}^3$ ,

$$H^1(\mathbb{R}^3) \xrightarrow{\nabla} H(\text{curl}; \mathbb{R}^3) \xrightarrow{\text{curl}} H(\text{div}; \mathbb{R}^3) \xrightarrow{\text{div}} L^2(\mathbb{R}^3) \quad (34)$$

at the discrete level, and to admit a sequence of projection operators  $\Pi^0, \dots, \Pi^3$  mapping infinite-dimensional function spaces into the discrete ones, such that the following diagram commutes:

$$\begin{array}{ccccccc} V^0 & \xrightarrow{\nabla} & V^1 & \xrightarrow{\text{curl}} & V^2 & \xrightarrow{\text{div}} & V^3 \\ \Pi^0 \downarrow & & \Pi^1 \downarrow & & \Pi^2 \downarrow & & \Pi^3 \downarrow \\ V_K^0 & \xrightarrow{\nabla} & V_K^1 & \xrightarrow{\text{curl}} & V_K^2 & \xrightarrow{\text{div}} & V_K^3 \end{array} \quad (35)$$

We point out that such commuting de Rham diagrams are a key tool in Finite Element Exterior Calculus (FEEC), see e.g. [6, 20, 2, 7, 8]. In our framework, it is these operators  $\Pi^\ell$ , together with the shape functions  $S$ , that will encode the coupling mechanism between the particles and the discrete fields. The bottom row thus consists of truncated Fourier spaces

$$\begin{aligned} V_K^0 &:= V_K^3 := \text{Span}(\{\Lambda_{\mathbf{k}} : \mathbf{k} \in \llbracket -K, K \rrbracket^3\}) \\ V_K^1 &:= V_K^2 := \text{Span}(\{\Lambda_{\mathbf{k}} \mathbf{e}_\alpha : \mathbf{k} \in \llbracket -K, K \rrbracket^3, \alpha \in \llbracket 1, 3 \rrbracket\}) \end{aligned}$$

where  $\mathbf{e}_\alpha$  is the unit basis vector in the  $\alpha$  dimension, and

$$\Lambda_{\mathbf{k}}(\mathbf{x}) := e^{\frac{2i\pi\mathbf{k}\cdot\mathbf{x}}{L}}, \quad \mathbf{x} \in [0, L]^3$$

is the Fourier basis function of index  $\mathbf{k} \in \mathbb{Z}^3$ . Using the fact that the discrete spaces  $V_K^1$  and  $V_K^2$  coincide in this spectral setting, we find that the weak discrete differential operators associated with the sequence (35) coincide with the strong (continuous) ones. As a consequence, the variational method derived in [9] takes the following form: the field equations read

$$\begin{cases} -\partial_t \mathbf{E}_K + \text{curl } \mathbf{B}_K = \Pi^2 \mathbf{J}_N^S \\ \partial_t \mathbf{B}_K + \text{curl } \mathbf{E}_K = 0 \end{cases} \quad \text{with} \quad \Pi^2 \mathbf{J}_N^S = \sum_{p=1 \dots N} q_p \Pi^2(\mathbf{V}_p S_{\mathbf{X}_p}) \quad (36)$$

with  $\mathbf{B}_K, \mathbf{E}_K$  in  $V_K^1 = V_K^2$ , and the particle trajectories read

$$\begin{cases} \frac{d}{dt} \mathbf{X}_p = \mathbf{V}_p \\ \frac{d}{dt} \mathbf{V}_p = \frac{q_p}{m_p} (\mathbf{E}^S(\mathbf{X}_p) + \mathbf{V}_p \times \mathbf{B}^S(\mathbf{X}_p)) \end{cases} \quad \text{with} \quad \begin{cases} E_\alpha^S(\mathbf{X}_p) = \int E_\alpha(\mathbf{x}) (\Pi_\alpha^2 S_{\mathbf{X}_p})(\mathbf{x}) d\mathbf{x} \\ B_\alpha^S(\mathbf{X}_p) = \int B_\alpha(\mathbf{x}) (\Pi_\alpha^1 S_{\mathbf{X}_p})(\mathbf{x}) d\mathbf{x} \end{cases} \quad (37)$$

for  $p \in \llbracket 1, N \rrbracket$  and  $\alpha \in \llbracket 1, 3 \rrbracket$ , with  $E_\alpha$  and  $B_\alpha$  the  $\alpha$ -components of  $\mathbf{E}_K$  and  $\mathbf{B}_K$ .

As for the operators  $\Pi^\ell$ , several choices can then be made that lead to a commuting diagram and each choice results in a different coupling mechanism between the particles and the fields. In [9] a set of projections was presented that is based on interpolation and hispolation, which in practice amounts to performing discrete Fourier transforms (DFT) on a grid with  $M = 2K + 1$  nodes but also involves surface and volume integrals of the particle shapes. In this article we will study two types of approximation operators:  $L^2$  projection operators corresponding to continuous Fourier transforms, as recalled in Section 3.4, and new pseudo-differential operators based on discrete Fourier transforms, that we present in Section 3.5. These choices will then respectively lead to two variational schemes with Hamiltonian structure, namely the gridless Particle-in-Fourier method, and a new spectral Fourier-GEMPIC method.

**Remark 1.** *Although we often follow the common usage and refer to  $\Pi^\ell$  as commuting projection operators, we emphasize that we do not require them to be actual projections in the sense that one would have  $\Pi^\ell = I$  on  $V_K^\ell$ . Indeed this property is not needed for the Hamiltonian structure of the resulting schemes [9], and by relaxing it we can directly extend our analysis to coupling methods that involve filtering or back-filtering mechanisms.*

### 3.2 Gauss and momentum-preserving variant

In [9], a variant of the abstract system (36)–(37) was also proposed, that is a priori not Hamiltonian but preserves both the Gauss laws and a discrete momentum. This modified system involves

the same operators from the general commuting diagram (35), and some interior products coupled with a dimension-dependent approximation operator  $\mathcal{A}_{h,\alpha}$ . Specifically, the momentum-preserving variant consists of the same field solver (36) as above, and of a modified particle pusher where the Lorentz term  $\mathbf{F}^S(\mathbf{X}_p, \mathbf{V}_p) = \mathbf{E}^S(\mathbf{X}_p) + \mathbf{V}_p \times \mathbf{B}^S(\mathbf{X}_p)$  from (37) is replaced by

$$\tilde{\mathbf{F}}^S(\mathbf{X}_p, \mathbf{V}_p) := \tilde{\mathbf{E}}^S(\mathbf{X}_p) + \tilde{\mathbf{R}}^S(\mathbf{X}_p, \mathbf{V}_p)$$

with components given by

$$\begin{cases} \tilde{E}_\alpha^S(\mathbf{X}_p) = \int E_\alpha(\mathbf{x})(\mathcal{A}_{h,\alpha}\Pi^3 S_{\mathbf{X}_p})(\mathbf{x}) \, d\mathbf{x} \\ \tilde{R}_\alpha^S(\mathbf{X}_p, \mathbf{V}_p) = \int \mathbf{B}_K(\mathbf{x}) \cdot (\mathcal{A}_{h,\alpha}(\mathbf{e}_\alpha \times \Pi^2(\mathbf{V}_p S_{\mathbf{X}_p})))(\mathbf{x}) \, d\mathbf{x}. \end{cases} \quad (38)$$

In the general construction of [9] the operator  $\mathcal{A}_{h,\alpha}$  was defined as a directional averaging on a grid with  $M$  points,  $h = L/M$ , which in Fourier space amounts to a diagonal filtering of the form  $(\mathcal{A}_{h,\alpha}G)_\mathbf{k} = \text{sinc}\left(\frac{2\pi\mathbf{k}\alpha}{M}\right)G_\mathbf{k}$ . This allows for the method to be well posed in general polynomial or spline finite element settings. With spectral solvers however, this averaging is not needed and one may simply take the identity operator,  $(\mathcal{A}_{h,\alpha}G)_\mathbf{k} = G_\mathbf{k}$ . We may then rewrite these pushing fields in terms of Fourier coefficients, for a clearer comparison. The fields in the Hamiltonian pusher (37) take the form

$$\begin{cases} E_\alpha^S(\mathbf{X}_p) = L^3 \sum_{\mathbf{k}} E_{\alpha,\mathbf{k}} \overline{(\Pi_\alpha^2 S_{\mathbf{X}_p})_\mathbf{k}} \\ R_\alpha^S(\mathbf{X}_p, \mathbf{V}_p) = \sum_{\nu=\pm 1} \nu V_{p,\alpha+\nu} B_{\alpha-\nu}(\mathbf{X}_p) = L^3 \sum_{\mathbf{k}} \sum_{\nu=\pm 1} \nu B_{\alpha-\nu,\mathbf{k}} V_{p,\alpha+\nu} \overline{(\Pi_{\alpha-\nu}^1 S_{\mathbf{X}_p})_\mathbf{k}}, \end{cases} \quad (39)$$

whereas the momentum-preserving ones read

$$\begin{cases} \tilde{E}_\alpha^S(\mathbf{X}_p) = L^3 \sum_{\mathbf{k}} E_{\alpha,\mathbf{k}} \overline{(\Pi^3 S_{\mathbf{X}_p})_\mathbf{k}} \\ \tilde{R}_\alpha^S(\mathbf{X}_p, \mathbf{V}_p) = L^3 \sum_{\mathbf{k}} \sum_{\nu=\pm 1} \nu B_{\alpha-\nu,\mathbf{k}} V_{p,\alpha+\nu} \overline{(\Pi_{\alpha+\nu}^2 S_{\mathbf{X}_p})_\mathbf{k}}. \end{cases} \quad (40)$$

In particular, we observe that the two schemes differ in the particle-field coupling operators involved in the pushing fields. After performing a convenient time discretization, we will see in Section 4.6 that this latter formulation will result in fully discrete PIC schemes with standard particle-field coupling terms, as described in Section 2.2.

### 3.3 Semi-discrete conservation properties

In [9] we have shown that the semi-discrete equations (36)–(37) have a discrete Hamiltonian structure, which in particular implies that they preserve the total energy and any discrete Casimir functional. In the particular setting of truncated Fourier spaces, a few basic conservation properties can be proven with a direct argument.

**Theorem 1.** *The variational spectral particle method (36)–(37) preserves the strong Gauss laws*

$$\begin{cases} \text{div } \mathbf{E}_K = \Pi^3 \rho_N^S \\ \text{div } \mathbf{B}_K = 0 \end{cases} \quad (41)$$

as well as the discrete energy

$$\mathcal{H}(t) = \frac{1}{2} \sum_{p=1}^N m_p |\mathbf{V}_p(t)|^2 + \frac{1}{2} \int_{[0,L]^3} \left( |\mathbf{E}_K(t, \mathbf{x})|^2 + |\mathbf{B}_K(t, \mathbf{x})|^2 \right) d\mathbf{x}. \quad (42)$$

If in addition the projection operators satisfy

$$\Pi_\alpha^1 = \Pi_\alpha^2 = \Pi_\alpha^3 \quad \text{for } 1 \leq \alpha \leq 3, \quad (43)$$

then it also preserves the discrete momentum

$$\mathcal{P}(t) = \sum_{p=1}^N m_p \mathbf{V}_p(t) + \int_{[0,L]^3} \mathbf{E}_K(t, \mathbf{x}) \times \mathbf{B}_K(t, \mathbf{x}) d\mathbf{x}. \quad (44)$$

*Proof.* The preservation of the magnetic Gauss law readily follows from the strong Faraday equation in (36). As for the electric Gauss law, we compute for an arbitrary smooth function  $\varphi$

$$\frac{d}{dt} \int \rho_N^S(t, \mathbf{x}) \varphi(\mathbf{x}) d\mathbf{x} = \sum_{p=1}^N q_p \int S(\tilde{\mathbf{x}}) \mathbf{V}_p \cdot \nabla \varphi(\tilde{\mathbf{x}} + \mathbf{X}_p) d\tilde{\mathbf{x}} = \int \mathbf{J}_N^S(t, \mathbf{x}) \cdot \nabla \varphi(\mathbf{x}) d\mathbf{x}$$

which shows that the continuity equation

$$\partial_t \rho_N^S + \operatorname{div} \mathbf{J}_N^S = 0 \quad (45)$$

always holds in distribution's sense. Taking next the divergence of the discrete Ampère equation in (36) the commuting diagram property (35) allows us to write

$$\partial_t \operatorname{div} \mathbf{E}_K = -\operatorname{div} \Pi^2 \mathbf{J}_N^S = -\Pi^3 \operatorname{div} \mathbf{J}_N^S = \partial_t \Pi^3 \rho_N^S$$

where the last equality follows from (45) and from the time-invariance of the operator  $\Pi^3$ . Integrating over time this shows that the electric Gauss law is indeed preserved. To show the energy conservation, we next compute using (36)

$$\frac{d}{dt} \left( \frac{1}{2} \int |\mathbf{E}_K|^2 + |\mathbf{B}_K|^2 \right) = \int \mathbf{E}_K \cdot (\nabla \times \mathbf{B}_K - \Pi^2 \mathbf{J}_N^S) - \mathbf{B}_K \cdot \nabla \times \mathbf{E}_K = - \int \mathbf{E}_K \cdot \Pi^2 \mathbf{J}_N^S$$

and, using (37),

$$\frac{d}{dt} \left( \frac{1}{2} \sum_{p=1}^N m_p |\mathbf{V}_p|^2 \right) = \sum_{p=1}^N q_p \int \Pi^2(\mathbf{V}_p S_{\mathbf{X}_p}) \cdot \mathbf{E}_K = \int \mathbf{E}_K \cdot \Pi^2 \mathbf{J}_N^S,$$

so that  $\mathcal{H}$  is indeed constant over time. We finally turn to the momentum conservation and assume that (43) holds. Then the coupling fields take the form

$$\mathbf{G}^S(\mathbf{X}_p) = \int \mathbf{G}_K(\mathbf{x}) (\Pi^3 S_{\mathbf{X}_p})(\mathbf{x}) d\mathbf{x} \quad \text{with } \mathbf{G} = \mathbf{E} \text{ or } \mathbf{B},$$

and the deposited current reads  $\Pi^2 \mathbf{J}_N^S = \sum_p q_p \Pi^2(\mathbf{V}_p S_{\mathbf{X}_p}) = \sum_p q_p \mathbf{V}_p \Pi^3(S_{\mathbf{X}_p})$ . Using (37) we compute

$$\frac{d}{dt} \sum_{p=1}^N m_p \mathbf{V}_p = \sum_{p=1}^N q_p \int (\mathbf{E}_K \Pi^3 S_{\mathbf{X}_p} + \mathbf{V}_p \times \mathbf{B}_K \Pi^3 S_{\mathbf{X}_p}) = \int \mathbf{E}_K \Pi^3 \rho_N^S + \int (\Pi^2 \mathbf{J}_N^S) \times \mathbf{B}_K,$$

and using (36) together with the identity  $\int_{\Omega} \mathbf{G} \times (\text{curl } \mathbf{G}) = \int_{\Omega} \nabla(\frac{1}{2} \mathbf{G}^2) - (\mathbf{G} \cdot \nabla) \mathbf{G} = \int_{\Omega} (\text{div } \mathbf{G}) \mathbf{G}$  valid for an arbitrary function  $\mathbf{G}$ , allows us to compute

$$\begin{aligned} \frac{d}{dt} \int_{\Omega} \mathbf{E}_K \times \mathbf{B}_K &= \int_{\Omega} (\text{curl } \mathbf{B}_K - \Pi^2 \mathbf{J}_N^S) \times \mathbf{B}_K - \int_{\Omega} \mathbf{E}_K \times (\text{curl } \mathbf{E}_K) \\ &= - \int_{\Omega} (\text{div } \mathbf{B}_K) \mathbf{B}_K - \int_{\Omega} \Pi^2 \mathbf{J}_N^S \times \mathbf{B}_K - \int_{\Omega} (\text{div } \mathbf{E}_K) \mathbf{E}_K \\ &= - \int_{\Omega} (\Pi^2 \mathbf{J}_N^S) \times \mathbf{B}_K - \int_{\Omega} (\Pi^3 \rho_K^S) \mathbf{E}_K \end{aligned}$$

where in the last equality we have used the Gauss laws (41). The result follows.  $\square$

### 3.4 Commuting projections using continuous Fourier transforms

Because truncated Fourier spaces have the particular property that they are stable under space differentiation,  $L^2$  projection operators can be used for the commuting diagram. This choice essentially corresponds to a gridless Particle-in-Fourier coupling described above, and in this article we will refer to the resulting method as a *Geometric Electromagnetic Particle-in-Fourier* (GEMPIF) method, to emphasize its natural expression in the general GEMPIC framework. In order to account for general filtering and back-filtering mechanisms, we consider an arbitrary collection of Hermitian coefficients  $\gamma_{\mathbf{k}} = \overline{\gamma_{-\mathbf{k}}} \in \mathbb{C}$ , and set

$$\Pi^0 := \Pi_{\alpha}^1 := \Pi_{\alpha}^2 := \Pi^3 \quad \text{for } \alpha \in \llbracket 1, 3 \rrbracket, \quad (46)$$

where  $\Pi^3$  is the operator that maps a function to its  $\gamma$ -filtered Fourier series of rank  $K$ ,

$$\Pi^3 G := \sum_{\mathbf{k} \in \llbracket -K, K \rrbracket^3} \gamma_{\mathbf{k}} \mathcal{F}_{\mathbf{k}}(G) \Lambda_{\mathbf{k}}, \quad (47)$$

with  $\mathcal{F}_{\mathbf{k}}$  the continuous Fourier coefficient operator, see (11). We observe that with unit filters  $\gamma_{\mathbf{k}} = 1$  the operators in (46) coincide with the  $L^2$  projection  $P_K$  on  $V^3 = V^0$ , characterized by

$$\int_{[0, L]^3} P_K G(\mathbf{x}) \overline{\Lambda_{\mathbf{k}}(\mathbf{x})} d\mathbf{x} = \int_{[0, L]^3} G(\mathbf{x}) \overline{\Lambda_{\mathbf{k}}(\mathbf{x})} d\mathbf{x} \quad \text{for } \mathbf{k} \in \llbracket -K, K \rrbracket^3.$$

For general filter coefficients we have the following result.

**Lemma 1.** *The filtered  $L^2$  projection operators  $\Pi^{\ell}$  defined by (46)–(47) satisfy the commuting diagram property (35) in a distribution sense, with periodic distributions as domain spaces:*

$$V^0 = V^3 = \mathcal{D}'_{\text{per}} \quad \text{and} \quad V^1 = V^2 = (\mathcal{D}'_{\text{per}})^3.$$

*Proof.* We may consider that  $\gamma_{\mathbf{k}} = 1$ , as the general case follows easily. The  $L^2$  projections over truncated Fourier spaces classically extend to periodic distributions [14], writing e.g.

$$\mathcal{F}_{\mathbf{k}}((\partial_{\alpha})^a \delta_{\mathbf{X}_p}) = \frac{(-1)^a}{L^3} \int_{[0, L]^3} \delta_{\mathbf{X}_p} (\partial_{\alpha})^a \overline{\Lambda_{\mathbf{k}}(\mathbf{x})} d\mathbf{x} = \left(\frac{1}{L}\right)^3 \left(\frac{2i\pi k_{\alpha}}{L}\right)^a e^{-\frac{2i\pi \mathbf{k} \cdot \mathbf{X}_p}{L}}$$

for  $\alpha \in \llbracket 1, 3 \rrbracket$  and  $a \in \mathbb{N}$ . The commuting diagram property is then derived from the symmetry of the discrete de Rham sequence. For instance, using that  $\text{div } V^1 = \text{div } V^2 \subset V^3 = V^0$  allows to write for all  $\mathbf{F} \in V^1$

$$\int (\nabla \Pi^0 G) \cdot \mathbf{F} = - \int (\Pi^0 G) \text{div } \mathbf{F} = - \int G \text{div } \mathbf{F} = \int (\nabla G) \cdot \mathbf{F} = \int (\Pi^1 \nabla G) \cdot \mathbf{F}$$

for any periodic distribution  $G \in \mathcal{D}'_{\text{per}}$ . Since  $\nabla V^0 \subset V^1$  this shows that  $\nabla \Pi^0 G = \Pi^1 \nabla G$ . The other relations  $\text{curl} \Pi^1 \mathbf{G} = \Pi^2 \text{curl} \mathbf{G}$  and  $\text{div} \Pi^2 \mathbf{G} = \Pi^3 \text{div} \mathbf{G}$  are proven in the same way.  $\square$

### 3.5 Commuting projections based on pseudo-differential DFT

In our framework, spectral PIC methods are obtained with commuting projection operators that involve discrete Fourier transforms on a finite grid. In [9] we have described a set of projections which rely on geometric degrees of freedom, namely nodal interpolations for  $V^0$  and edge, face, and volume ‘‘histopolations’’ for  $V^1$ ,  $V^2$ , and  $V^3$ , respectively. As a result the current deposition involves face integrals which need to be integrated over the particle trajectories, which somehow deviates from standard PIC methods where common deposition procedures are based on point evaluations of the particle shapes. For this reason we consider here an alternate construction based on a new sequence of projection operators, obtained by combining DFT coefficients on a grid with  $M \geq 2K + 1$  nodes as in Section 2.2 with standard derivatives and anti-derivatives in Fourier variables. As we will see, these new projections will lead to deposition methods that only involve pointwise evaluations of the particle shapes. Following the terminology of [23], we will refer to the resulting methods as *Fourier-Geometric Electromagnetic Particle-in-Cell* (Fourier-GEMPIC) methods. Beginning with the space  $V^3$ , we let

$$\Pi^3 G = \sum_{\mathbf{k} \in [-K, K]^3} (\Pi^3 G)_{\mathbf{k}} \Lambda_{\mathbf{k}} \quad (48)$$

be defined on  $\mathcal{C}_{\text{per}}^0$  the space of continuous,  $L$ -periodic functions, by its coefficients

$$(\Pi^3 G)_{\mathbf{k}} := \gamma_{\mathbf{k}} \tilde{\mathcal{F}}_{M, \mathbf{k}}(G) := \gamma_{\mathbf{k}} \tilde{\mathcal{F}}_{M, k_1} \otimes \tilde{\mathcal{F}}_{M, k_2} \otimes \tilde{\mathcal{F}}_{M, k_3}(G). \quad (49)$$

Here, the values  $\gamma_{\mathbf{k}} = \overline{\gamma_{-\mathbf{k}}} \in \mathbb{C}$  are again Hermitian filters, and the univariate operators  $\tilde{\mathcal{F}}_{M, k_\alpha}$  are defined as

$$\tilde{\mathcal{F}}_{M, k_\alpha}(G) := \begin{cases} \frac{1}{L} \int_0^L G(x_\alpha) dx_\alpha & \text{if } k_\alpha = 0 \\ \mathcal{F}_{M, k_\alpha}(G) = \frac{1}{M} \sum_{m_\alpha=1}^M G(m_\alpha h) e^{-\frac{2i\pi k_\alpha m_\alpha}{M}} & \text{if } k_\alpha \neq 0. \end{cases} \quad (50)$$

We note that for  $\gamma_0 = 1$  the operator  $\Pi^3$  is a *conservative* discrete Fourier transform, indeed

$$\int_{[0, L]^3} \Pi^3 G(\mathbf{x}) d\mathbf{x} = L^3 (\Pi^3 G)_0 = L^3 \tilde{\mathcal{F}}_{M, \mathbf{0}}(G) = \int_{[0, L]^3} G(\mathbf{x}) d\mathbf{x}.$$

For the vector-valued  $V^2$  we then set

$$\Pi^2 \mathbf{G} = \sum_{\alpha=1}^3 \sum_{\mathbf{k} \in [-K, K]^3} (\Pi_\alpha^2 G_\alpha)_{\mathbf{k}} \Lambda_{\mathbf{k}} \mathbf{e}_\alpha \quad \text{with} \quad (\Pi_\alpha^2 G_\alpha)_{\mathbf{k}} := \gamma_{\mathbf{k}} (\hat{D}_{\mathbf{k}, \alpha})^{-1} \tilde{\mathcal{F}}_{M, \mathbf{k}}(\tilde{D}_{\mathbf{k}, \alpha} G_\alpha),$$

with pseudo-differential operators defined as

$$\hat{D}_{\mathbf{k}, \alpha} c_{\mathbf{k}} := \begin{cases} c_{\mathbf{k}} & \text{if } k_\alpha = 0 \\ \frac{2i\pi k_\alpha}{L} c_{\mathbf{k}} & \text{if } k_\alpha \neq 0 \end{cases} \quad \text{and} \quad \tilde{D}_{\mathbf{k}, \alpha} G := \begin{cases} G & \text{if } k_\alpha = 0 \\ \partial_\alpha G & \text{if } k_\alpha \neq 0 \end{cases} \quad (51)$$

for any  $c_{\mathbf{k}} \in \mathbb{C}$  and any function  $\mathbf{G}$  in the anisotropic regularity space  $\mathcal{C}_{\text{per}, 1}^1 \times \mathcal{C}_{\text{per}, 2}^1 \times \mathcal{C}_{\text{per}, 3}^1$ , where we have denoted

$$\mathcal{C}_{\text{per}, \alpha}^1 := \{G \in \mathcal{C}_{\text{per}}^0 : \partial_\alpha G \in \mathcal{C}_{\text{per}}^0\}. \quad (52)$$

Similarly for the vector-valued space  $V^1$  we define (using a circular convention  $\alpha \equiv \alpha + 3$  for the dimension indices)

$$\left\{ \begin{array}{l} \Pi^1 \mathbf{G} = \sum_{\alpha=1}^3 \sum_{\mathbf{k} \in \llbracket -K, K \rrbracket^3} (\Pi_\alpha^1 G_\alpha)_{\mathbf{k}} \Lambda_{\mathbf{k}} \mathbf{e}_\alpha \\ \text{with } (\Pi_\alpha^1 G_\alpha)_{\mathbf{k}} := \gamma_{\mathbf{k}} (\hat{D}_{\mathbf{k}, \alpha+1} \hat{D}_{\mathbf{k}, \alpha+2})^{-1} \tilde{\mathcal{F}}_{M, \mathbf{k}} (\tilde{D}_{\mathbf{k}, \alpha+1} \tilde{D}_{\mathbf{k}, \alpha+2} G_\alpha) \end{array} \right.$$

for any function  $\mathbf{G}$  in the anisotropic regularity space  $\mathcal{C}_{\text{per}, 2, 3}^1 \times \mathcal{C}_{\text{per}, 1, 3}^1 \times \mathcal{C}_{\text{per}, 1, 2}^1$ , where

$$\mathcal{C}_{\text{per}, \alpha, \beta}^1 := \{G \in \mathcal{C}_{\text{per}}^0 : \partial_\alpha \partial_\beta G \in \mathcal{C}_{\text{per}}^0\}. \quad (53)$$

Finally for the scalar-valued space  $V^0$  we define

$$\left\{ \begin{array}{l} \Pi^0 G = \sum_{\mathbf{k} \in \llbracket -K, K \rrbracket^3} (\Pi^0 G)_{\mathbf{k}} \Lambda_{\mathbf{k}} \\ \text{with } (\Pi^0 G)_{\mathbf{k}} := \gamma_{\mathbf{k}} (\hat{D}_{\mathbf{k}, 1} \hat{D}_{\mathbf{k}, 2} \hat{D}_{\mathbf{k}, 3})^{-1} \tilde{\mathcal{F}}_{M, \mathbf{k}} (\tilde{D}_{\mathbf{k}, 1} \tilde{D}_{\mathbf{k}, 2} \tilde{D}_{\mathbf{k}, 3} G), \end{array} \right.$$

for all  $G$  in the anisotropic regularity space

$$\mathcal{C}_{\text{per}, 1, 2, 3}^1 := \{G \in \mathcal{C}_{\text{per}}^0 : \partial_1 \partial_2 \partial_3 G \in \mathcal{C}_{\text{per}}^0\}. \quad (54)$$

**Lemma 2.** *The above pseudo-differential operators  $\Pi^\ell$  satisfy the commuting diagram property (35) with domains defined as*

$$V^0 = \mathcal{C}_{\text{per}, 1, 2, 3}^1, \quad V^1 = \mathcal{C}_{\text{per}, 2, 3}^1 \times \mathcal{C}_{\text{per}, 1, 3}^1 \times \mathcal{C}_{\text{per}, 1, 2}^1, \quad V^2 = \mathcal{C}_{\text{per}, 1}^1 \times \mathcal{C}_{\text{per}, 2}^1 \times \mathcal{C}_{\text{per}, 3}^1, \quad V^3 = \mathcal{C}_{\text{per}}^0.$$

Moreover if  $\gamma_{\mathbf{k}} = 1$ , they are projection operators on their respective Fourier spaces.

*Proof.* The projection property can be checked by direct computation. To verify the commuting diagram property we consider again the case  $\gamma_{\mathbf{k}} = 1$ , as the general case follows easily. We begin with the last relation and observe that

$$\tilde{\mathcal{F}}_{M, \mathbf{k}} (\partial_\alpha G_\alpha) = \frac{2i\pi k_\alpha}{L} (\Pi^2 \mathbf{G})_{\mathbf{k}, \alpha}$$

holds for every dimension  $\alpha \in \llbracket 1, 3 \rrbracket$  and mode  $\mathbf{k} \in \mathbb{Z}^3$ : this follows from the definition of  $\Pi^2$  if  $k_\alpha \neq 0$ , and from that of the conservative Fourier transform  $\tilde{\mathcal{F}}_{M, \mathbf{k}}$  if  $k_\alpha = 0$ . We then have, for an arbitrary  $\mathbf{k}$ ,

$$(\Pi^3 \operatorname{div} \mathbf{G})_{\mathbf{k}} = \sum_{\alpha} (\Pi^3 (\partial_\alpha G_\alpha))_{\mathbf{k}} = \sum_{\alpha} \tilde{\mathcal{F}}_{M, \mathbf{k}} (\partial_\alpha G_\alpha) = \sum_{\alpha} \frac{2i\pi k_\alpha}{L} (\Pi^2 \mathbf{G})_{\mathbf{k}, \alpha} = (\operatorname{div} \Pi^2 \mathbf{G})_{\mathbf{k}}$$

which shows that  $\Pi^3 \operatorname{div} = \operatorname{div} \Pi^2$  holds on  $V^2$ . Similarly, for all  $\mathbf{k}$  and  $\alpha$ , we have

$$\begin{aligned} (\Pi^2 \operatorname{curl} \mathbf{G})_{\mathbf{k}, \alpha} &= (\Pi_\alpha^2 (\partial_{\alpha+1} G_{\alpha+2} - \partial_{\alpha+2} G_{\alpha+1}))_{\mathbf{k}} \\ &= (\hat{D}_{\mathbf{k}, \alpha})^{-1} \tilde{\mathcal{F}}_{M, \mathbf{k}} (\tilde{D}_{\mathbf{k}, \alpha} (\partial_{\alpha+1} G_{\alpha+2} - \partial_{\alpha+2} G_{\alpha+1})) \\ &= \frac{2i\pi k_{\alpha+1}}{L} (\Pi^1 \mathbf{G})_{\mathbf{k}, \alpha+2} - \frac{2i\pi k_{\alpha+2}}{L} (\Pi^1 \mathbf{G})_{\mathbf{k}, \alpha+1} = (\operatorname{curl} \Pi^1 \mathbf{G})_{\mathbf{k}, \alpha} \end{aligned}$$

so that  $\Pi^2 \operatorname{curl} = \operatorname{curl} \Pi^1$  holds on  $V^1$ . Finally we compute, again for all  $\mathbf{k}, \alpha$ ,

$$\begin{aligned} (\Pi^1 \nabla G)_{\mathbf{k}, \alpha} &= (\Pi_\alpha^1 \partial_\alpha G)_{\mathbf{k}} = (\hat{D}_{\mathbf{k}, \alpha+1} \hat{D}_{\mathbf{k}, \alpha+2})^{-1} \tilde{\mathcal{F}}_{M, \mathbf{k}} (\tilde{D}_{\mathbf{k}, \alpha+1} \tilde{D}_{\mathbf{k}, \alpha+2} \partial_\alpha G) \\ &= \frac{2i\pi k_\alpha}{L} (\Pi^0 G)_{\mathbf{k}} = (\nabla \Pi^0 G)_{\mathbf{k}, \alpha} \end{aligned}$$

which shows that  $\Pi^1 \nabla = \nabla \Pi^0$  holds on  $V^0$  and ends the proof.  $\square$

### 3.6 GEMPIF and Fourier-GEMPIC methods

Now that we have defined two sets of projection operators  $\Pi^\ell$  with commuting diagram properties, we may specify the spectral variational scheme (36)–(37). As announced above, the Geometric Particle-in-Fourier (GEMPIF) method corresponds to the case where the operators  $\Pi^\ell$  are defined as the  $L^2$  projections of Section 3.4. Then any periodic distribution  $S \in \mathcal{D}'_{\text{per}}$  is admissible and the coupling terms take the form

$$\mathbf{J}_{\mathbf{k}}^S = \gamma_{\mathbf{k}} \sum_{p=1 \dots N} q_p \mathbf{V}_p \mathcal{F}_{\mathbf{k}}(S_{\mathbf{X}_p}) = \gamma_{\mathbf{k}} \mathcal{F}_{\mathbf{k}}(S) \sum_{p=1 \dots N} q_p \mathbf{V}_p e^{-\frac{2i\pi \mathbf{k} \cdot \mathbf{X}_p}{L}} \quad (55)$$

and

$$\begin{cases} E_{\alpha}^S(\mathbf{X}_p) = L^3 \sum_{\mathbf{k} \in [-K, K]^3} \overline{\gamma_{\mathbf{k}}} E_{\alpha, \mathbf{k}} \overline{\mathcal{F}_{\mathbf{k}}(S_{\mathbf{X}_p})} = L^3 \sum_{\mathbf{k} \in [-K, K]^3} \overline{\gamma_{\mathbf{k}} \mathcal{F}_{\mathbf{k}}(S)} E_{\alpha, \mathbf{k}} e^{\frac{2i\pi \mathbf{k} \cdot \mathbf{X}_p}{L}} \\ B_{\alpha}^S(\mathbf{X}_p) = L^3 \sum_{\mathbf{k} \in [-K, K]^3} \overline{\gamma_{\mathbf{k}}} B_{\alpha, \mathbf{k}} \overline{\mathcal{F}_{\mathbf{k}}(S_{\mathbf{X}_p})} = L^3 \sum_{\mathbf{k} \in [-K, K]^3} \overline{\gamma_{\mathbf{k}} \mathcal{F}_{\mathbf{k}}(S)} B_{\alpha, \mathbf{k}} e^{\frac{2i\pi \mathbf{k} \cdot \mathbf{X}_p}{L}}. \end{cases} \quad (56)$$

Up to the arbitrary filter coefficients  $\gamma_{\mathbf{k}}$ , this corresponds to the gridless coupling of Section 2.1.

With the pseudo-differential operators defined in Section 3.5, the coupling terms involve modified Fourier coefficients such as  $(\Pi_{\alpha}^2 S_{\mathbf{X}_p})_{\mathbf{k}} = (\hat{D}_{\mathbf{k}, \alpha})^{-1} \tilde{\mathcal{F}}_{M, \mathbf{k}}(\hat{D}_{\mathbf{k}, \alpha} S_{\mathbf{X}_p})$ , see (51), and similar coefficients for  $\Pi_{\alpha}^1 S_{\mathbf{X}_p}$ , involving derivatives along dimensions  $\alpha + 1$  and  $\alpha - 1$ . The resulting coupling terms read then

$$J_{\alpha, \mathbf{k}}^S = \gamma_{\mathbf{k}} \left( \frac{2i\pi k_{\alpha}}{L} \right)^{-1} \left( \frac{1}{M} \right)^3 \sum_{p, \mathbf{m}} q_p v_{p, \alpha} \partial_{\alpha} S(\mathbf{m}h - \mathbf{X}_p) e^{-\frac{2i\pi \mathbf{k} \cdot \mathbf{m}}{M}} \quad (57)$$

and

$$\begin{cases} E_{\alpha}^S(\mathbf{X}_p) = \overline{\gamma_{\mathbf{k}}} h^3 \sum_{\mathbf{k}, \mathbf{m}} E_{\alpha, \mathbf{k}} \left( \frac{-2i\pi k_{\alpha}}{L} \right)^{-1} \partial_{\alpha} S(\mathbf{m}h - \mathbf{X}_p) e^{\frac{2i\pi \mathbf{k} \cdot \mathbf{m}}{M}} \\ B_{\alpha}^S(\mathbf{X}_p) = \overline{\gamma_{\mathbf{k}}} h^3 \sum_{\mathbf{k}, \mathbf{m}} B_{\alpha, \mathbf{k}} \left( \frac{-2i\pi k_{\alpha+1}}{L} \right)^{-1} \left( \frac{-2i\pi k_{\alpha-1}}{L} \right)^{-1} \partial_{\alpha+1} \partial_{\alpha-1} S(\mathbf{m}h - \mathbf{X}_p) e^{\frac{2i\pi \mathbf{k} \cdot \mathbf{m}}{M}} \end{cases} \quad (58)$$

with the modifications specified in (49)–(51) when  $k_{\alpha} = 0$  or  $k_{\alpha \pm 1} = 0$ . We observe that in order to be admissible, shape functions need to be in the mixed  $C^1$  space (54). For tensor-product B-splines this corresponds to using at least quadratic splines in each dimension.

Although these terms involve a DFT grid, they differ from the standard spectral PIC coupling terms recalled in Section 2.2, which are not associated with a variational principle. For the purpose of comparison we rewrite the latter in the case of a general  $\gamma$ -filtering,

$$J_{\alpha, \mathbf{k}}^S = \gamma_{\mathbf{k}} \left( \frac{1}{M} \right)^3 \sum_{p, \mathbf{m}} q_p v_{p, \alpha} S(\mathbf{m}h - \mathbf{X}_p) e^{-\frac{2i\pi \mathbf{k} \cdot \mathbf{m}}{M}} \quad (59)$$

and

$$\begin{cases} E_{\alpha}^S(\mathbf{X}_p) = \overline{\gamma_{\mathbf{k}}} h^3 \sum_{\mathbf{k}, \mathbf{m}} E_{\alpha, \mathbf{k}} S(\mathbf{m}h - \mathbf{X}_p) e^{\frac{2i\pi \mathbf{k} \cdot \mathbf{m}}{M}} \\ B_{\alpha}^S(\mathbf{X}_p) = \overline{\gamma_{\mathbf{k}}} h^3 \sum_{\mathbf{k}, \mathbf{m}} B_{\alpha, \mathbf{k}} S(\mathbf{m}h - \mathbf{X}_p) e^{\frac{2i\pi \mathbf{k} \cdot \mathbf{m}}{M}}. \end{cases} \quad (60)$$

Below we will see how these differences translate in a fully discrete setting.



## 4 Fully discrete schemes based on Hamiltonian time splitting

In this section we specify some fully discrete schemes for the variational semi-discrete systems described above. As these schemes are derived from a Hamiltonian splitting procedure, it will be convenient to first rewrite the general equations (36)–(37) in a matrix form.

### 4.1 Matrix formulation of the semi-discrete Hamiltonian system

Similarly as in [9, 23], we gather the degrees of freedom of the discrete solution into multi-index arrays. Particle unknowns will be written as

$$\mathbf{X} = (X_{p,\alpha})_{(p,\alpha) \in \llbracket 1, N \rrbracket \times \llbracket 1, 3 \rrbracket}, \quad \mathbf{V} = (V_{p,\alpha})_{(p,\alpha) \in \llbracket 1, N \rrbracket \times \llbracket 1, 3 \rrbracket} \in \mathbb{R}^{3N},$$

(with an implicit time-dependance) and electro-magnetic field coefficients will be denoted by

$$\mathbf{E} = (E_{\alpha,\mathbf{k},\sigma})_{(\alpha,\mathbf{k},\sigma) \in \llbracket 1, 3 \rrbracket \times \llbracket -K, K \rrbracket^3 \times \llbracket 0, 1 \rrbracket}, \quad \mathbf{B} = (B_{\alpha,\mathbf{k},\sigma})_{(\alpha,\mathbf{k},\sigma) \in \llbracket 1, 3 \rrbracket \times \llbracket -K, K \rrbracket^3 \times \llbracket 0, 1 \rrbracket} \in \mathbb{R}^{6(2K+1)^3}$$

where each component-wise Fourier coefficient is decomposed into its real and imaginary parts,

$$G_{\alpha,\mathbf{k}} = G_{\alpha,\mathbf{k},0} + iG_{\alpha,\mathbf{k},1} \quad \text{with } G = E \text{ or } B.$$

For notational reasons it is convenient to see these arrays as column vectors (with an arbitrary ordering of the multi-indices), and to gather them into a global array of time-dependent unknowns,

$$\mathbf{U} = \begin{pmatrix} \mathbf{X} \\ \mathbf{V} \\ \mathbf{E} \\ \mathbf{B} \end{pmatrix}. \quad (61)$$

We may then rewrite the equations of the geometric Fourier-particle method (36)–(37) in terms of these coefficients. Using the fact that the vector-valued operators  $\Pi^\ell$  are defined component-wise, in the sense that their component along any dimension  $\alpha \in \llbracket 1, 3 \rrbracket$  reads

$$(\Pi^\ell(\mathbf{G}))_\alpha = \Pi_\alpha^\ell(G_\alpha) \quad (62)$$

for some scalar operators  $\Pi_\alpha^\ell$ , we may rewrite the particle trajectories as

$$\begin{cases} \frac{d}{dt} X_{p,\alpha} = V_{p,\alpha} \\ \frac{d}{dt} V_{p,\alpha} = L^3 \frac{q_p}{m_p} \sum_{\mathbf{k}} \left( E_{\alpha,\mathbf{k}} \overline{(\Pi_\alpha^2 S_{\mathbf{X}_p})_{\mathbf{k}}} \pm V_{p,\alpha \mp 1} B_{\alpha \mp 1, \mathbf{k}} \overline{(\Pi_{\alpha \mp 1}^1 S_{\mathbf{X}_p})_{\mathbf{k}}} \right) \\ \quad = L^3 \frac{q_p}{m_p} \sum_{\mathbf{k}, \sigma} \left( E_{\alpha,\mathbf{k},\sigma} (\Pi_\alpha^2 S_{\mathbf{X}_p})_{\mathbf{k},\sigma} \pm V_{p,\alpha \pm 1} B_{\alpha \mp 1, \mathbf{k}, \sigma} (\Pi_{\alpha \mp 1}^1 S_{\mathbf{X}_p})_{\mathbf{k},\sigma} \right) \end{cases} \quad (63)$$

for all  $p \in \llbracket 1, N \rrbracket$  and  $\alpha \in \llbracket 1, 3 \rrbracket$ . Here we have used the fact that the right-hand side is real, and we recall the circular convention ( $\alpha \equiv \alpha + 3$ ) for the dimension indices. In terms of the above arrays, this gives

$$\begin{cases} \frac{d}{dt} \mathbf{X} = \mathbf{V} \\ \frac{d}{dt} \mathbf{V} = \mathbb{W}_{\frac{q}{m}} (\mathbb{S}^2(\mathbf{X}) \mathbb{M}^2 \mathbf{E} + \mathbb{R}(\mathbf{X}, \mathbf{B}) \mathbf{V}) \end{cases}$$

where  $\mathbb{W}_{\frac{q}{m}} = \text{diag}(\frac{q_p}{m_p} : p \in \llbracket 1, N \rrbracket)$  is the diagonal weighting matrix carrying the particles charge to mass ratios,  $\mathbb{S}^2(\mathbf{X})$  is the  $\Pi^2$  Fourier-particle coupling matrix,

$$\mathbb{S}^2(\mathbf{X})_{(p,\beta),(\alpha,\mathbf{k},\sigma)} = \delta_{\alpha,\beta} (\Pi_\alpha^2 S_{\mathbf{X}_p})_{\mathbf{k},\sigma},$$

$\mathbb{M}^\ell = L^3 \mathbb{I}_{N_\ell}$  is the (diagonal) finite element ‘‘mass’’ matrix for the Fourier basis in  $V_K^\ell$ , and  $\mathbb{R}(\mathbf{X}, \mathbf{B})$  is the skew-symmetric matrix corresponding to magnetic rotation,

$$\begin{aligned} \mathbb{R}(\mathbf{X}, \mathbf{B})_{(p,\alpha),(p',\beta)} &= \delta_{p,p'} \sum_{\mathbf{k},\sigma} L^3 (\delta_{\alpha+1,\beta} B_{\alpha-1,\mathbf{k},\sigma} (\Pi_{\alpha-1}^1 S_{\mathbf{X}_p})_{\mathbf{k},\sigma} - \delta_{\alpha-1,\beta} B_{\alpha+1,\mathbf{k},\sigma} (\Pi_{\alpha+1}^1 S_{\mathbf{X}_p})_{\mathbf{k},\sigma}) \\ &= \delta_{p,p'} \sum_{\nu=\pm 1} \delta_{\alpha+\nu,\beta} \int \nu B_{\alpha-\nu}(\mathbf{x}) (\Pi_{\alpha-\nu}^1 S_{\mathbf{X}_p})(\mathbf{x}) \, d\mathbf{x}. \end{aligned} \quad (64)$$

As for the Maxwell solver, we first rewrite (36) in terms of (complex) Fourier coefficients, namely

$$\begin{cases} \frac{d}{dt} E_{\alpha,\mathbf{k}} = \sum_{\nu=\pm 1} \nu \frac{2i\pi}{L} k_{\alpha+\nu} B_{\alpha-\nu,\mathbf{k}} - \sum_p q_p v_{p,\alpha} \Pi_\alpha^2(S_{\mathbf{X}_p})_{\mathbf{k}} \\ \frac{d}{dt} B_{\alpha,\mathbf{k}} = - \sum_{\nu=\pm 1} \nu \frac{2i\pi}{L} k_{\alpha+\nu} E_{\alpha-\nu,\mathbf{k}} \end{cases} \quad (65)$$

for  $\mathbf{k} \in \llbracket -K, K \rrbracket^3$  and  $\alpha \in \llbracket 1, 3 \rrbracket$ . In terms of the above arrays, this rewrites as

$$\begin{cases} \frac{d}{dt} \mathbf{E} = \mathbb{C} \mathbf{B} - \mathbb{S}_2(\mathbf{X})^T \mathbb{W}_q \mathbf{V} \\ \frac{d}{dt} \mathbf{B} = -\mathbb{C} \mathbf{E} \end{cases} \quad (66)$$

with  $\mathbb{C}$  the symmetric matrix of the curl operator, which writes here

$$\mathbb{C}_{(\alpha,\mathbf{k},\sigma),(\beta,\ell,\tau)} = \delta_{\mathbf{k},\ell} (1 - \delta_{\sigma,\tau}) (-1)^{\sigma+1} \frac{2\pi}{L} (\delta_{\alpha-1,\beta} k_{\alpha+1} - \delta_{\alpha+1,\beta} k_{\alpha-1}).$$

Writing next the discrete Hamiltonian (42) as a function of the array variable (61),

$$\mathcal{H}(\mathbf{U}) = \frac{1}{2} \mathbf{V}^\top \mathbb{W}_m \mathbf{V} + \frac{1}{2} \mathbf{E}^\top \mathbb{M}^2 \mathbf{E} + \frac{1}{2} \mathbf{B}^\top \mathbb{M}^1 \mathbf{B} \quad (67)$$

we find for the corresponding derivatives

$$\nabla_{\mathbf{U}} \mathcal{H}(\mathbf{U}) = \begin{pmatrix} \nabla_{\mathbf{X}} \mathcal{H} \\ \nabla_{\mathbf{V}} \mathcal{H} \\ \nabla_{\mathbf{E}} \mathcal{H} \\ \nabla_{\mathbf{B}} \mathcal{H} \end{pmatrix} (\mathbf{U}) = \begin{pmatrix} \mathbf{0} \\ \mathbb{W}_m \mathbf{V} \\ \mathbb{M}^2 \mathbf{E} \\ \mathbb{M}^1 \mathbf{B} \end{pmatrix}$$

and this allows us to rewrite the abstract spectral particle method (36)–(37) in the form of a non-canonical Hamiltonian system

$$\frac{d}{dt} \mathbf{U} = \mathbb{J}(\mathbf{U}) \nabla_{\mathbf{U}} \mathcal{H}(\mathbf{U}) \quad (68)$$

with

$$\mathbb{J}(\mathbf{U}) = \mathbb{J}(\mathbf{X}, \mathbf{B}) = \begin{pmatrix} 0 & \mathbb{W}_{\frac{1}{m}} & 0 & 0 \\ -\mathbb{W}_{\frac{1}{m}} & \mathbb{W}_{\frac{q}{m}} \mathbb{R}(\mathbf{X}, \mathbf{B}) \mathbb{W}_{\frac{1}{m}} & \mathbb{W}_{\frac{q}{m}} \mathbb{S}_2(\mathbf{X}) & 0 \\ 0 & -\mathbb{S}_2(\mathbf{X})^T \mathbb{W}_{\frac{q}{m}} & 0 & \mathbb{C}(M^1)^{-1} \\ 0 & 0 & -(M^1)^{-1} \mathbb{C} & 0 \end{pmatrix}. \quad (69)$$

In [9] we have shown that  $\mathbb{J}$  is a Poisson matrix in the sense of [17, Def. VII.2.4], i.e., it is skew-symmetric and it satisfies the matrix Jacobi identity. In particular, System (68) may be rewritten in the usual form

$$\frac{d}{dt} \mathbf{U} = \{\mathbf{U}, \mathcal{H}\}$$

with a discrete Poisson bracket given by  $\{\mathcal{F}, \mathcal{G}\} = (\nabla_{\mathbf{U}} \mathcal{F})^T \mathbb{J} \nabla_{\mathbf{U}} \mathcal{G}$ .

## 4.2 Hamiltonian splitting time discretization

Following [17, 10], we now apply a splitting procedure to the semi-discrete Hamiltonian system (68). This will provide us with a series of Hamiltonian structure-preserving schemes of various orders in time, for the variational Fourier-particle equations (36)–(37).

Similarly as in [19, 23], we split the kinetic part along the three different dimensions, but keep together the electric and magnetic parts as we are solving the Maxwell equations in Fourier spaces. This leads us to the following Hamiltonian splitting,

$$\mathcal{H} = \sum_{\alpha=1}^3 \mathcal{H}_{v_\alpha} + \mathcal{H}_{EB} \quad (70)$$

with

$$\mathcal{H}_{v_\alpha}(\mathbf{U}) := \sum_{p=1}^N \frac{m_p}{2} |V_{p,\alpha}|^2 \quad \text{and} \quad \mathcal{H}_{EB}(\mathbf{U}) := \frac{1}{2} \int_{\Omega} \left( |\mathbf{E}_K(\mathbf{x})|^2 + |\mathbf{B}_K(\mathbf{x})|^2 \right) d\mathbf{x}$$

where we remind that  $\mathbf{U}$  carries the time dependent coefficients of the full solution, see (61). This splitting has two key properties. It leads to split steps that can all be solved exactly, and it preserve the fact that  $\mathbb{J}(\mathbf{X}, \mathbf{B})$  is a Poisson matrix, see Theorem 2. As a consequence, we know that any combination of the split steps will provide a Hamiltonian time scheme which preserves the Casimir invariants and the total energy up to some constant time discretization error, see e.g. [17]. Specifically, we decompose System (68) into the subsystems,

$$\frac{d}{dt} \mathbf{U}(t) = \mathbb{J}(\mathbf{U}) \nabla_{\mathbf{U}} \mathcal{H}_{v_\alpha}(\mathbf{U}) \quad \text{for} \quad \alpha \in \llbracket 1, 3 \rrbracket \quad (71)$$

and

$$\frac{d}{dt} \mathbf{U}(t) = \mathbb{J}(\mathbf{U}) \nabla_{\mathbf{U}} \mathcal{H}_{EB}(\mathbf{U}). \quad (72)$$

Denoting by  $\varphi_{\tau, v_\alpha}$  and  $\varphi_{\tau, EB}$  the corresponding solution flow maps, we can use standard composition methods to obtain time integrators of various orders, as described e.g. in [23]: either a first order Lie-Trotter scheme

$$\Phi_{\Delta t, L} = \varphi_{\Delta t, EB} \circ \varphi_{\Delta t, v_3} \circ \varphi_{\Delta t, v_2} \circ \varphi_{\Delta t, v_1}$$

or a second-order Strang scheme

$$\Phi_{\Delta t, S2} = \varphi_{\Delta t/2, L} \circ \varphi_{\Delta t/2, L}^* \quad (73)$$

where  $\varphi_{\tau, L}^* := \varphi_{-\tau, L}^{-1}$  denotes the adjoint flow. Since each split flow is the exact solution of an autonomous system they are all self-adjoint, *i.e.* symmetric, which yields

$$\Phi_{\Delta t, S2} = \varphi_{\Delta t/2, EB} \circ \varphi_{\Delta t/2, v_3} \circ \varphi_{\Delta t/2, v_2} \circ \varphi_{\Delta t, v_1} \circ \varphi_{\Delta t/2, v_2} \circ \varphi_{\Delta t/2, v_3} \circ \varphi_{\Delta t/2, EB}.$$

Similarly we can use a fourth-order Suzuki-Yoshida scheme

$$\varphi_{\Delta t, S4} = \varphi_{\gamma_1 \Delta t, S2} \circ \varphi_{\gamma_2 \Delta t, S2} \circ \varphi_{\gamma_1 \Delta t, S2} \quad (74)$$

with  $\gamma_1 = 1/(2 - 2^{1/3})$  and  $\gamma_2 = -2^{1/3}/(2 - 2^{1/3})$ , or higher-order composition methods, see e.g. [27, 17].

In the sections below we specify the resulting equations for each split step, and we provide an explicit solution for the GEMPIF and Fourier-GEMPIC methods described in Section 3.6.

### 4.3 Discrete Hamiltonian subsystems

Before giving the solutions we detail the subsystems (71) and (72).

**Kinetic  $\mathcal{H}_{v_\alpha}$  subsystems.** For each dimension  $\alpha \in \llbracket 1, 3 \rrbracket$ , System (71) reads

$$\left\{ \begin{array}{l} \frac{d}{dt} \mathbf{X} = \mathbf{V}^{[\alpha]} \\ \frac{d}{dt} \mathbf{V} = \mathbb{W}_{\frac{q}{m}} \mathbb{R}(\mathbf{X}, \mathbf{B}) \mathbf{V}^{[\alpha]} \\ \frac{d}{dt} \mathbf{E} = -\mathbb{S}_2(\mathbf{X})^T \mathbb{W}_q \mathbf{V}^{[\alpha]} \\ \frac{d}{dt} \mathbf{B} = 0 \end{array} \right. \quad \text{i.e.,} \quad \left\{ \begin{array}{l} \frac{d}{dt} \mathbf{X}_p = \mathbf{V}_p^{[\alpha]} \\ \frac{d}{dt} \mathbf{V}_p = \frac{q_p}{m_p} \mathbf{V}_p^{[\alpha]} \times \mathbf{B}^S(\mathbf{X}_p) \\ \frac{d}{dt} \mathbf{E}_K = -\Pi^2(\mathbf{J}_N^{S, [\alpha]}) \\ \frac{d}{dt} \mathbf{B}_K = 0 \end{array} \right.$$

(for all  $p$ ), where we have denoted  $\mathbf{V}_p^{[\alpha]} = e_\alpha V_{p,\alpha}$  and similarly for  $\mathbf{V}^{[\alpha]}$ ,  $\mathbf{J}_N^{S, [\alpha]}$ . Expressed in scalar coefficients and using the definition (37) of  $\mathbf{B}^S$ , this gives (again with the circular convention  $\alpha \equiv \alpha + 3$  on dimension indices)

$$\left\{ \begin{array}{l} \frac{d}{dt} X_{p,\alpha} = V_{p,\alpha} \\ \frac{d}{dt} X_{p,\alpha+\nu} = 0 \\ \frac{d}{dt} V_{p,\alpha} = 0 \\ \frac{d}{dt} V_{p,\alpha+\nu} = -\nu \frac{q_p}{m_p} L^3 \sum_{\mathbf{k}} V_{p,\alpha} B_{\alpha-\nu,\mathbf{k}} \overline{(\Pi_{\alpha-\nu}^1 S_{\mathbf{X}_p})_{\mathbf{k}}} \\ \frac{d}{dt} E_{\alpha,\mathbf{k}} = -\sum_p q_p V_{p,\alpha} (\Pi_\alpha^2 S_{\mathbf{X}_p})_{\mathbf{k}} \\ \frac{d}{dt} E_{\alpha+\nu,\mathbf{k}} = 0 \\ \frac{d}{dt} \mathbf{B}_{\mathbf{k}} = 0 \end{array} \right. \quad (75)$$

for all  $p \in \llbracket 1, N \rrbracket$ ,  $\mathbf{k} \in \llbracket -K, K \rrbracket^3$  and  $\nu = \pm 1$ .

**Electromagnetic  $\mathcal{H}_{EB}$  subsystems.** For the electromagnetic part, System (72) reads

$$\left\{ \begin{array}{l} \frac{d}{dt} \mathbf{X} = 0 \\ \frac{d}{dt} \mathbf{V} = \mathbb{W}_{\frac{q}{m}} \mathbb{S}_2(\mathbf{X}) \mathbb{M}^2 \mathbf{E} \\ \frac{d}{dt} \mathbf{E} = \mathbb{C} \mathbf{B} \\ \frac{d}{dt} \mathbf{B} = -\mathbb{C} \mathbf{E} \end{array} \right. \quad \text{i.e.,} \quad \left\{ \begin{array}{l} \frac{d}{dt} \mathbf{X}_p = 0 \\ \frac{d}{dt} \mathbf{V}_p = \frac{q_p}{m_p} \mathbf{E}^S(\mathbf{X}_p) \\ \frac{d}{dt} \mathbf{E}_K = \text{curl } \mathbf{B}_K \\ \frac{d}{dt} \mathbf{B}_K = -\text{curl } \mathbf{E}_K \end{array} \right.$$

for all  $p \in \llbracket 1, N \rrbracket$ . Using scalar coefficients and the definition (37) of  $\mathbf{E}^S$ , this reads

$$\left\{ \begin{array}{l} \frac{d}{dt} \mathbf{X}_p = 0 \\ \frac{d}{dt} V_{p,\alpha} = \frac{q_p}{m_p} L^3 \sum_{\mathbf{k}} E_{\alpha,\mathbf{k}} \overline{(\Pi_\alpha^2 S_{\mathbf{X}_p})_{\mathbf{k}}} \\ \frac{d}{dt} \mathbf{E}_{\mathbf{k}} = \frac{2i\pi\mathbf{k}}{L} \times \mathbf{B}_{\mathbf{k}} \\ \frac{d}{dt} \mathbf{B}_{\mathbf{k}} = -\frac{2i\pi\mathbf{k}}{L} \times \mathbf{E}_{\mathbf{k}} \end{array} \right. \quad (76)$$

for all  $\alpha \in \llbracket 1, 3 \rrbracket$ ,  $p \in \llbracket 1, N \rrbracket$  and  $\mathbf{k} \in \llbracket -K, K \rrbracket^3$ . This splitting enjoys the following properties.

**Theorem 2.** *All the split steps above preserve the discrete Gauss laws (41), namely*

$$\operatorname{div} \mathbf{E}_K = \Pi^3 \rho_N = \sum_{p=1}^N q_p \Pi^3 S_{\mathbf{X}_p} \quad \text{and} \quad \operatorname{div} \mathbf{B}_K = 0 \quad (77)$$

and the fact that  $\mathbb{J}(\mathbf{X}, \mathbf{B})$  is a Poisson bracket. In particular, any combination of the individual flows  $\varphi_{\tau, v_\alpha}$  and  $\varphi_{\tau, EB}$  preserves the discrete Hamiltonian structure. If in addition the operators  $\Pi^\ell$  satisfy (43), then the discrete momentum (44) is also preserved exactly.

*Proof.* By applying the computations from the proof of Theorem 1 to any of the split steps, one verifies that the discrete Gauss laws are preserved, as well as the discrete momentum in the case where (43) holds. In particular the Gauss law  $\operatorname{div} \mathbf{B}_K = 0$  is preserved, so that Theorem 1 from [9] applies and this shows that  $\mathbb{J}$  defines a discrete Poisson bracket at each split step. The standard theory of Hamiltonian splitting schemes then applies, see [17].  $\square$

#### 4.4 Explicit steps for the GEMPIF method

In the GEMPIF method the operators  $\Pi^\ell$  are defined as  $L^2$  projections with general filter coefficients  $\gamma_{\mathbf{k}}$ , see Section 3.4. In particular we have

$$(\Pi_\alpha^1 S_{\mathbf{X}_p})_{\mathbf{k}} = (\Pi_\alpha^2 S_{\mathbf{X}_p})_{\mathbf{k}} = \left(\frac{1}{L}\right)^3 \gamma_{\mathbf{k}} \int_{\Omega} S(\mathbf{x} - \mathbf{X}_p) e^{-\frac{2i\pi \mathbf{k} \cdot \mathbf{x}}{L}} d\mathbf{x} = \gamma_{\mathbf{k}} \mathcal{F}_{\mathbf{k}}(S) e^{-\frac{2i\pi \mathbf{k} \cdot \mathbf{X}_p}{L}} \quad (78)$$

for any direction  $\alpha \in \llbracket 1, 3 \rrbracket$ . This allows us to give explicit solutions for each split subsystem.

##### Directional kinetic steps.

**Lemma 3.** *In the GEMPIF method, the exact solution  $\varphi_{\tau, v_\alpha} : \mathbf{U}^0 \rightarrow \mathbf{U}(\tau)$  of the kinetic split step (75) in a direction  $\alpha \in \llbracket 1, 3 \rrbracket$  is given by the explicit expressions*

$$\varphi_{\tau, v_\alpha} : \left\{ \begin{array}{l} X_{p,\alpha}(\tau) = X_{p,\alpha}^0 + \tau V_{p,\alpha} \\ X_{p,\alpha+\nu}(\tau) = X_{p,\alpha+\nu}^0 \\ V_{p,\alpha}(\tau) = V_{p,\alpha}^0 \\ V_{p,\alpha+\nu}(\tau) = V_{p,\alpha+\nu}^0 - \nu \tau \frac{q_p}{m_p} L^3 \sum_{\mathbf{k} \in \llbracket -K, K \rrbracket^3} B_{\alpha-\nu, \mathbf{k}} \overline{\left( \gamma_{\mathbf{k}} \mathcal{F}_{\mathbf{k}}(S) \hat{V}_{p,\alpha, \mathbf{k}}(\tau) \right)} \\ E_{\alpha, \mathbf{k}}(\tau) = E_{\alpha, \mathbf{k}}^0 - \tau \gamma_{\mathbf{k}} \mathcal{F}_{\mathbf{k}}(S) \sum_{p=1 \dots N} q_p \hat{V}_{p,\alpha, \mathbf{k}}(\tau) \\ E_{\alpha+\nu, \mathbf{k}}(\tau) = E_{\alpha+\nu, \mathbf{k}}^0 \\ \mathbf{B}_K(\tau) = \mathbf{B}_K^0. \end{array} \right.$$

for all  $p \in \llbracket 1, N \rrbracket$ ,  $\mathbf{k} \in \llbracket -K, K \rrbracket^3$  and  $\nu = \pm 1$ , with

$$\hat{V}_{p,\alpha, \mathbf{k}}(\tau) := \begin{cases} V_{p,\alpha} e^{-\frac{2i\pi \mathbf{k} \cdot \mathbf{X}_p^0}{L}} & \text{if } k_\alpha = 0 \\ \left( -\frac{2i\pi k_\alpha \tau}{L} \right)^{-1} \left( e^{-\frac{2i\pi k_\alpha \tau V_{p,\alpha}}{L}} - 1 \right) e^{-\frac{2i\pi \mathbf{k} \cdot \mathbf{X}_p^0}{L}} & \text{if } k_\alpha \neq 0. \end{cases} \quad (79)$$

*Proof.* In (75), the velocity equations read

$$\frac{d}{dt}V_{p,\alpha+\nu} = -\nu \frac{q_p}{m_p} L^3 \sum_{\mathbf{k}} B_{\alpha-\nu,\mathbf{k}} \overline{\left( \gamma_{\mathbf{k}} \mathcal{F}_{\mathbf{k}}(S) V_{p,\alpha} e^{-\frac{2i\pi\mathbf{k}\cdot\mathbf{X}_p}{L}} \right)}$$

and for the electric field we have

$$\frac{d}{dt}E_{\mathbf{k},\alpha} = -\gamma_{\mathbf{k}} \mathcal{F}_{\mathbf{k}}(S) \sum_p q_p V_{p,\alpha} e^{-\frac{2i\pi\mathbf{k}\cdot\mathbf{X}_p}{L}}.$$

Since the only time-varying term in the right hand sides is  $\frac{d}{dt}\mathbf{X}_p(t) = \mathbf{V}_p^{[\alpha]} = V_{p,\alpha}\mathbf{e}_\alpha$ , we integrate

$$\int_0^\tau V_{p,\alpha} e^{-\frac{2i\pi\mathbf{k}\cdot\mathbf{X}_p(t)}{L}} dt = \tau \hat{V}_{p,\alpha,\mathbf{k}}(\tau)$$

with the expression in (79), which proves the lemma.  $\square$

**Electromagnetic step.** In (76) the source-free Maxwell equations have an explicit solution (see e.g. [35]), which allows to solve also for the particles. The resulting flow takes the form

$$\varphi_{\tau,EB} : \begin{cases} \mathbf{X}_p(\tau) = \mathbf{X}_p^0 \\ V_{p,\alpha}(\tau) = V_{p,\alpha}^0 + \frac{q_p}{m_p} L^3 \sum_{\mathbf{k} \in \llbracket -K, K \rrbracket^3} \left( \int_0^\tau E_{\alpha,\mathbf{k}}(t) dt \right) \overline{(\Pi_\alpha^2 S_{\mathbf{X}_p^0})_{\mathbf{k}}} \\ \mathbf{E}_{\mathbf{k}}(\tau) = \mathbf{E}_{\mathbf{k}}^0 + \hat{\mathbf{k}} \times \left( (1 - c(\tau))(\hat{\mathbf{k}} \times \mathbf{E}_{\mathbf{k}}^0) + i s(\tau) \mathbf{B}_{\mathbf{k}}^0 \right) \\ \mathbf{B}_{\mathbf{k}}(\tau) = \mathbf{B}_{\mathbf{k}}^0 + \hat{\mathbf{k}} \times \left( (1 - c(\tau))(\hat{\mathbf{k}} \times \mathbf{B}_{\mathbf{k}}^0) - i s(\tau) \mathbf{E}_{\mathbf{k}}^0 \right) \end{cases} \quad (80)$$

for all  $p \in \llbracket 1, N \rrbracket$ ,  $\alpha \in \llbracket 1, 3 \rrbracket$  and  $\mathbf{k} \in \llbracket -K, K \rrbracket^3$ . Here the projected shaped particle is given by (78), and the integrated electric field reads

$$\int_0^\tau \mathbf{E}_{\mathbf{k}}(t) dt = \tau \mathbf{E}_{\mathbf{k}}^0 + \hat{\mathbf{k}} \times \left( \left( \tau - \frac{L}{2\pi|\mathbf{k}|} s(\tau) \right) (\hat{\mathbf{k}} \times \mathbf{E}_{\mathbf{k}}^0) + i \frac{L}{2\pi|\mathbf{k}|} (1 - c(\tau)) \mathbf{B}_{\mathbf{k}}^0 \right) \quad (81)$$

where we have set

$$c(\tau) = \cos\left(\frac{2\pi|\mathbf{k}|\tau}{L}\right), \quad s(\tau) = \sin\left(\frac{2\pi|\mathbf{k}|\tau}{L}\right) \quad \text{with} \quad |\mathbf{k}| = (\mathbf{k} \cdot \mathbf{k})^{\frac{1}{2}}, \quad (82)$$

and  $\hat{\mathbf{k}} := \mathbf{k}/|\mathbf{k}|$  if  $\mathbf{k} \neq 0$ , otherwise  $\hat{\mathbf{k}} := 0$ .

## 4.5 Explicit steps for the Fourier-GEMPIC method

We now consider the Fourier-GEMPIC method defined by the pseudo-differential DFT operators from Section 3.5.

**Directional kinetic steps.** We have the following result.

**Lemma 4.** For the operators  $\Pi^\ell$  defined as in Section 3.5, the exact solution  $\varphi_{\tau, v_\alpha} : \mathbf{U}^0 \rightarrow \mathbf{U}(\tau)$  to the kinetic split step (75) in a direction  $\alpha \in \llbracket 1, 3 \rrbracket$  is given by the explicit expressions

$$\varphi_{\tau, v_\alpha} : \begin{cases} X_{p,\alpha}(\tau) = X_{p,\alpha}^0 + \tau V_{p,\alpha} \\ X_{p,\alpha+\nu}(\tau) = X_{p,\alpha+\nu}^0 \\ V_{p,\alpha}(\tau) = V_{p,\alpha}^0 \\ V_{p,\alpha+\nu}(\tau) = V_{p,\alpha+\nu}^0 - \nu \tau \frac{q_p}{m_p} L^3 \sum_{\mathbf{k} \in \llbracket -K, K \rrbracket^3} B_{\alpha-\nu, \mathbf{k}} \overline{\hat{V}_{p,\alpha, \mathbf{k}}^{2,\nu}(\tau)} \\ E_{\alpha, \mathbf{k}}(\tau) = E_{\alpha, \mathbf{k}}^0 - \tau \sum_{p=1 \dots N} q_p \hat{V}_{p,\alpha, \mathbf{k}}^3(\tau) \\ E_{\alpha+\nu, \mathbf{k}}(\tau) = E_{\alpha+\nu, \mathbf{k}}^0 \\ \mathbf{B}_{\mathbf{k}}(\tau) = \mathbf{B}_{\mathbf{k}}^0 \end{cases} \quad (83)$$

for all  $p \in \llbracket 1, N \rrbracket$ ,  $\mathbf{k} \in \llbracket -K, K \rrbracket^3$  and  $\nu = \pm 1$ , with

$$\hat{V}_{p,\alpha, \mathbf{k}}^{2,\nu}(\tau) := \begin{cases} V_{p,\alpha}(\Pi_{\alpha+\nu}^2 S_{\mathbf{X}_p^0})_{\mathbf{k}} & \text{if } k_\alpha = 0 \\ -\left(\frac{2i\pi k_\alpha}{L}\right)^{-1} \frac{1}{\tau} [(\Pi_{\alpha+\nu}^2 S_{\mathbf{X}_p})_{\mathbf{k}}]_0^\tau & \text{if } k_\alpha \neq 0 \end{cases} \quad (84)$$

and

$$\hat{V}_{p,\alpha, \mathbf{k}}^3(\tau) := \begin{cases} V_{p,\alpha}(\Pi^3 S_{\mathbf{X}_p^0})_{\mathbf{k}} & \text{if } k_\alpha = 0 \\ -\left(\frac{2i\pi k_\alpha}{L}\right)^{-1} \frac{1}{\tau} [(\Pi^3 S_{\mathbf{X}_p})_{\mathbf{k}}]_0^\tau & \text{if } k_\alpha \neq 0. \end{cases} \quad (85)$$

*Proof.* We remind the velocity equation from (75),

$$\frac{d}{dt} V_{p,\alpha+\nu} = -\nu \frac{q_p}{m_p} L^3 \sum_{\mathbf{k}} B_{\alpha-\nu, \mathbf{k}} V_{p,\alpha} \overline{(\Pi_{\alpha-\nu}^1 S_{\mathbf{X}_p})_{\mathbf{k}}}$$

and the electric one,

$$\frac{d}{dt} E_{\alpha, \mathbf{k}} = - \sum_p q_p V_{p,\alpha} (\Pi_\alpha^2 S_{\mathbf{X}_p})_{\mathbf{k}}.$$

Here by definition of the pseudo-differential projection operators, we have

$$(\Pi_{\alpha-\nu}^1 S_{\mathbf{X}_p})_{\mathbf{k}} = \gamma_{\mathbf{k}} \hat{D}_{\mathbf{k}, \alpha}^{-1} \hat{D}_{\mathbf{k}, \alpha+\nu}^{-1} \tilde{\mathcal{F}}_{M, \mathbf{k}}(\tilde{D}_{\mathbf{k}, \alpha} \tilde{D}_{\mathbf{k}, \alpha+\nu} S_{\mathbf{X}_p}) \quad (86)$$

and

$$(\Pi_\alpha^2 S_{\mathbf{X}_p})_{\mathbf{k}} = \gamma_{\mathbf{k}} \hat{D}_{\mathbf{k}, \alpha}^{-1} \tilde{\mathcal{F}}_{M, \mathbf{k}}(\tilde{D}_{\mathbf{k}, \alpha} S_{\mathbf{X}_p}). \quad (87)$$

We begin with the term involving  $\Pi^2$  as the computations are simpler. We first observe that if  $k_\alpha = 0$ , then

$$V_{p,\alpha}(\Pi_\alpha^2 S_{\mathbf{X}_p})_{\mathbf{k}} = \gamma_{\mathbf{k}} V_{p,\alpha} \tilde{\mathcal{F}}_{M, \mathbf{k}}(S_{\mathbf{X}_p}) = V_{p,\alpha}(\Pi^3 S_{\mathbf{X}_p})_{\mathbf{k}}$$

and this quantity is constant, since the conservative DFT coefficient is an integral along  $\mathbf{e}_\alpha$ . Next if  $k_\alpha \neq 0$ , we compute

$$\begin{aligned}
V_{p,\alpha}(\Pi_\alpha^2 S_{\mathbf{X}_p})_{\mathbf{k}} &= \gamma_{\mathbf{k}} \left( \frac{2i\pi k_\alpha}{L} \right)^{-1} V_{p,\alpha} \tilde{\mathcal{F}}_{M,\mathbf{k}}(\partial_\alpha S_{\mathbf{X}_p}) \\
&= \gamma_{\mathbf{k}} \left( \frac{2i\pi k_\alpha}{L} \right)^{-1} \frac{V_{p,\alpha}}{M^3} \sum_{\mathbf{m}} \partial_\alpha S(\mathbf{m}h - \mathbf{X}_p(t)) e^{-\frac{2i\pi \mathbf{k} \cdot \mathbf{m}}{M}} \\
&= -\gamma_{\mathbf{k}} \left( \frac{2i\pi k_\alpha}{L} \right)^{-1} \frac{1}{M^3} \sum_{\mathbf{m}} \frac{d}{dt} \left( S(\mathbf{m}h - \mathbf{X}_p(t)) \right) e^{-\frac{2i\pi \mathbf{k} \cdot \mathbf{m}}{M}} \\
&= -\left( \frac{2i\pi k_\alpha}{L} \right)^{-1} \frac{d}{dt} (\Pi^3 S_{\mathbf{X}_p})_{\mathbf{k}}.
\end{aligned}$$

It follows that we can integrate exactly  $\int_0^\tau V_{p,\alpha}(\Pi_\alpha^2 S_{\mathbf{X}_p})_{\mathbf{k}} dt = \tau \hat{V}_{p,\alpha,\mathbf{k}}^3(\tau)$  with the expression from (85), which provides the update of  $E_{\alpha,\mathbf{k}}$ . Turning to the terms involving  $\Pi^1$  we observe that if  $k_\alpha = 0$ , then

$$V_{p,\alpha}(\Pi_{\alpha-\nu}^1 S_{\mathbf{X}_p})_{\mathbf{k}} = \gamma_{\mathbf{k}} V_{p,\alpha} \hat{D}_{\mathbf{k},\alpha+\nu}^{-1} \tilde{\mathcal{F}}_{M,\mathbf{k}}(\tilde{D}_{\mathbf{k},\alpha+\nu} S_{\mathbf{X}_p}) = V_{p,\alpha}(\Pi_{\alpha+\nu}^2 S_{\mathbf{X}_p})_{\mathbf{k}}$$

and again this quantity is constant, for the same reason as above. Now if  $k_\alpha \neq 0$ , then using  $\frac{d}{dt} \mathbf{X}_p(t) = \mathbf{V}_p^{[\alpha]} = V_{p,\alpha} \mathbf{e}_\alpha$  we compute

$$\begin{aligned}
V_{p,\alpha}(\Pi_{\alpha-\nu}^1 S_{\mathbf{X}_p})_{\mathbf{k}} &= \gamma_{\mathbf{k}} \left( \frac{2i\pi k_\alpha}{L} \right)^{-1} V_{p,\alpha} \hat{D}_{\mathbf{k},\alpha+\nu}^{-1} \tilde{\mathcal{F}}_{M,\mathbf{k}}(\partial_\alpha \tilde{D}_{\mathbf{k},\alpha+\nu} S_{\mathbf{X}_p}) \\
&= \gamma_{\mathbf{k}} \left( \frac{2i\pi k_\alpha}{L} \right)^{-1} \hat{D}_{\mathbf{k},\alpha+\nu}^{-1} \frac{V_{p,\alpha}}{M^3} \sum_{\mathbf{m}} \partial_\alpha \tilde{D}_{\mathbf{k},\alpha+\nu} S(\mathbf{m}h - \mathbf{X}_p(t)) e^{-\frac{2i\pi \mathbf{k} \cdot \mathbf{m}}{M}} \\
&= -\gamma_{\mathbf{k}} \left( \frac{2i\pi k_\alpha}{L} \right)^{-1} \hat{D}_{\mathbf{k},\alpha+\nu}^{-1} \frac{1}{M^3} \sum_{\mathbf{m}} \frac{d}{dt} \left( \tilde{D}_{\mathbf{k},\alpha+\nu} S(\mathbf{m}h - \mathbf{X}_p(t)) \right) e^{-\frac{2i\pi \mathbf{k} \cdot \mathbf{m}}{M}} \\
&= -\left( \frac{2i\pi k_\alpha}{L} \right)^{-1} \frac{d}{dt} (\Pi_{\alpha+\nu}^2 S_{\mathbf{X}_p})_{\mathbf{k}}.
\end{aligned}$$

It follows that  $\int_0^\tau V_{p,\alpha}(\Pi_{\alpha-\nu}^1 S_{\mathbf{X}_p})_{\mathbf{k}} dt = \tau \hat{V}_{p,\alpha,\mathbf{k}}^{2,\nu}(\tau)$ , now with the expression from (84). This gives the update for  $V_{p,\alpha+\nu}$ .  $\square$

**Electromagnetic step.** The exact solution flow  $\varphi_{\tau,EB}$  is again given by (80)–(82), up to replacing the  $\Pi^2$  projected term in (80) by its specific expression, see (87).

#### 4.6 A Gauss and momentum preserving Fourier-PIC scheme

By applying the same splitting method as above to the momentum and Gauss preserving scheme presented in Section 3.2, we obtain a standard Fourier-PIC coupling as described in Section 2.2, as follows. For the kinetic subsystem (75) along  $\alpha$ , the modification from (39) to (40) applies to  $\alpha \leftarrow \alpha + \nu$  and amounts to replacing the operator  $\Pi_{\alpha-\nu}^1$  by  $\Pi_\alpha^2$ . For the electromagnetic



subsystem (76) it just amounts to replacing  $\Pi_\alpha^2$  by  $\Pi^3$ . The modified equations read then

$$\left\{ \begin{array}{l} \frac{d}{dt} X_{p,\alpha} = V_{p,\alpha} \\ \frac{d}{dt} X_{p,\alpha+\nu} = 0 \\ \frac{d}{dt} V_{p,\alpha} = 0 \\ \frac{d}{dt} V_{p,\alpha+\nu} = -\nu \frac{q_p}{m_p} L^3 \sum_{\mathbf{k}} V_{p,\alpha} B_{\alpha-\nu,\mathbf{k}} \overline{(\Pi_\alpha^2 S_{X_p})_{\mathbf{k}}} \\ \frac{d}{dt} E_{\alpha,\mathbf{k}} = - \sum_p q_p V_{p,\alpha} (\Pi_\alpha^2 S_{X_p})_{\mathbf{k}} \\ \frac{d}{dt} E_{\alpha+\nu,\mathbf{k}} = 0 \\ \frac{d}{dt} \mathbf{B}_{\mathbf{k}} = 0 \end{array} \right. \quad \text{and} \quad \left\{ \begin{array}{l} \frac{d}{dt} \mathbf{X}_p = 0 \\ \frac{d}{dt} \mathbf{V}_p = \frac{q_p}{m_p} L^3 \sum_{\mathbf{k}} \mathbf{E}_{\mathbf{k}} \overline{(\Pi^3 S_{X_p})_{\mathbf{k}}} \\ \frac{d}{dt} \mathbf{E}_{\mathbf{k}} = \frac{2i\pi\mathbf{k}}{L} \times \mathbf{B}_{\mathbf{k}} \\ \frac{d}{dt} \mathbf{B}_{\mathbf{k}} = -\frac{2i\pi\mathbf{k}}{L} \times \mathbf{E}_{\mathbf{k}}, \end{array} \right.$$

and explicit solutions are obtained by computing as in the proof of Lemma 4. For the kinetic subsystem along  $\alpha$ , the flow  $\varphi_{\tau,v_\alpha}$  is given by

$$\varphi_{\tau,v_\alpha} : \left\{ \begin{array}{l} X_{p,\alpha}(\tau) = X_{p,\alpha}^0 + \tau V_{p,\alpha} \\ X_{p,\alpha+\nu}(\tau) = X_{p,\alpha+\nu}^0 \\ V_{p,\alpha}(\tau) = V_{p,\alpha}^0 \\ V_{p,\alpha+\nu}(\tau) = V_{p,\alpha+\nu}^0 - \nu\tau \frac{q_p}{m_p} L^3 \sum_{\mathbf{k} \in \llbracket -K, K \rrbracket^3} B_{\alpha-\nu,\mathbf{k}} \widehat{V}_{p,\alpha,\mathbf{k}}^3(\tau) \\ E_{\alpha,\mathbf{k}}(\tau) = E_{\alpha,\mathbf{k}}^0 - \tau \sum_p q_p \widehat{V}_{p,\alpha,\mathbf{k}}^3(\tau) \\ E_{\alpha+\nu,\mathbf{k}}(\tau) = E_{\alpha+\nu,\mathbf{k}}^0 \\ \mathbf{B}_K(\tau) = \mathbf{B}_K^0 \end{array} \right.$$

where we remind that  $\widehat{V}_{p,\alpha,\mathbf{k}}^3(\tau)$  is defined in (85). For the electromagnetic step the flow  $\varphi_{\tau,EB}$  corresponds to (80)–(82) with a modified velocity equation, namely

$$V_{p,\alpha}(\tau) = V_{p,\alpha}^0 + \frac{q_p}{m_p} L^3 \sum_{\mathbf{k} \in \llbracket -K, K \rrbracket^3} \left( \int_0^\tau E_{\alpha,\mathbf{k}}(t) dt \right) \overline{(\Pi^3 S_{X_p^0})_{\mathbf{k}}}. \quad (88)$$

In particular, we see that the fully discrete steps all involve the operator  $\Pi^3$ , see (49), which corresponds to the standard DFT coupling described in Section 2.2, up to the use of exact integrals (50) along zero-modes. This scheme does not have a Hamiltonian structure, but it satisfies some important conservation properties.

**Lemma 5.** *The Fourier-PIC scheme described above preserves the discrete Gauss laws (41) and the discrete momentum (44).*

*Proof.* The proof is a matter of elementary computations, similar to the ones involved in the proofs of Theorem 1. One key observation is that the above modifications in the velocity equations have no effect on the Gauss laws being preserved, and they precisely lead to an exact momentum preservation.  $\square$

## 4.7 Summary of the proposed methods

In the above sections we have derived geometric Fourier-particle methods following the Discrete Action Principle formalized in [9], where the coupling between the fields and the particles is represented by abstract projection operators on the truncated Fourier spaces that satisfy a commuting diagram property. This results in semi-discrete schemes that preserve the Gauss laws and have a discrete Hamiltonian structure relying on a non-canonical Poisson bracket.

When the coupling operators are defined as  $L^2$  projections, the coupling is gridless and essentially relies on continuous Fourier coefficients. The resulting method preserves the total momentum in addition to the charge and energy, and corresponds to the Particle-In-Fourier (PIF) approach. Here it is called GEMPIF to emphasize its geometric nature.

When the coupling operators are defined as pseudo-differential DFT projections, the coupling involves a grid and essentially relies on discrete Fourier coefficients. The resulting method can be seen as a variant of standard spectral PIC methods and is called Fourier-GEMPIC.

Fully discrete schemes of various orders in time have then been constructed by a Hamiltonian splitting procedure. These schemes are Poisson maps, in particular they preserve the discrete Poisson bracket and a modified energy that approximates the exact one to the time order of the splitting.

Finally we have observed that Fourier-PIC schemes with standard coupling terms can be obtained as a variant of the above Fourier-GEMPIC method. These schemes are not Hamiltonian, but they preserve exactly the Gauss laws and the total momentum.

Since our approach handles general shape functions  $S$  and arbitrary filter coefficients  $\gamma_{\mathbf{k}}$ , we may use high order shapes with anti-aliasing properties in the Fourier-GEMPIC methods, and the ad-hoc *back-filtering* procedure (28)–(30) to avoid the damping of relevant modes in the computational range.

## 5 Numerical illustration in 1D2V and 1D1V

In this section we present some numerical results obtained with several of the methods described above. Specifically, we will compare

- the GEMPIF scheme described in Section 4.4 with point shape functions ( $S = \delta$ ),
- the Fourier-GEMPIC scheme described in Section 4.5, involving a DFT grid with  $M$  points and B-spline shapes of degree  $\kappa$ . To assess the benefits of back-filtering, we will use two versions of this scheme: a plain *smoothed Fourier* SF-GEMPIC method corresponding to  $\gamma_{\mathbf{k}} = 1$ , and a *back-filtered Fourier* BFF-GEMPIC method that involves filter coefficients

$$\gamma_{\mathbf{k}} := \frac{1}{\sigma_{\mathbf{k}}} = \prod_{\alpha=1}^3 \left( \text{sinc} \left( \frac{\pi k_{\alpha}}{\mu(2K+1)} \right) \right)^{-(\kappa+1)} \quad \text{with} \quad \mu := \frac{M}{2K+1} \geq 1 \quad (89)$$

where we remind that  $\mu$  is the oversampling parameter, see (24).

- the Fourier-PIC scheme described in Section 4.6, which also uses a DFT grid with  $M$  points and B-spline shapes of degree  $\kappa$ . Similarly as above, this scheme will be used in two versions, namely a basic *smoothed Fourier* SF-PIC method corresponding to  $\gamma_{\mathbf{k}} = 1$ , and a *back-filtered Fourier* BFF-PIC method involving the coefficients (89).

## 5.1 Periodic plasma test-cases

For our numerical experiments we consider a periodic one-species model in 1D2V and 1D1V similarly as in [9], with zero-mean current to preserve the total momentum, i.e.

$$\partial_t E_1 = -J_1 + \frac{1}{L_1} \int_0^{L_1} J_1, \quad \partial_t E_2 + \partial_{x_1} B_3 = -J_2 + \frac{1}{L_1} \int_0^{L_1} J_1, \quad \partial_t B_3 + \partial_{x_1} E_3 = 0,$$

and standard plasma test-cases: classical **Landau damping** test-cases corresponding to

$$f^0(x, v_1) = (1 + \epsilon \cos(kx)) \frac{1}{\sqrt{2\pi}} \exp\left(-\frac{v_1^2}{2}\right)$$

with  $k = 0.5$  and  $\epsilon = 0.5$  or  $0.01$  for the strong and weak damping, a standard **Weibel instability** [39, 23] where

$$f^0(x, v_1, v_2) = \frac{1}{2\pi\sigma_1\sigma_2} \exp\left(-\frac{1}{2}\left(\frac{v_1^2}{\sigma_1^2} + \frac{v_2^2}{\sigma_2^2}\right)\right)$$

and where the initial magnetic field is  $B_3(t = 0, x_1) = \beta \cos(kx_1)$ , with  $\sigma_1 = 0.02/\sqrt{2}$  and  $\sigma_2 = \sqrt{12}\sigma_1$ ,  $\beta = 10^{-4}$  and  $k = 1.25$ , a **two-stream instability**

$$f^0(x, v_1) = (1 + \epsilon \cos(kx)) \frac{1}{2\sqrt{2\pi}} \left( \exp\left(-\frac{(v_1 + 2.4)^2}{2}\right) - \exp\left(-\frac{(v_1 - 2.4)^2}{2}\right) \right)$$

with  $\epsilon = 5 \cdot 10^{-4}$  and  $k = 0.2$ , and a **bump-on-tail instability** corresponding to

$$f^0(x, v_1) = (1 + \epsilon \cos(kx)) \frac{1}{\sqrt{2\pi}} \left( \delta \exp\left(-\frac{v_1^2}{2}\right) + 2(1 - \delta) \exp\left(-2(v_1 - 3.5)^2\right) \right)$$

with  $\delta = 0.9$ ,  $\epsilon = 5 \cdot 10^{-3}$  and  $k = 0.3$ . For these test-cases the domain size is  $L_1 = \frac{2\pi}{k}$ , except for the last one where we take  $L_1 = \frac{4\pi}{k}$ . The initial  $B_3$  field is zero unless stated otherwise, and the initial  $\mathbf{E}$  field is computed from the particles by solving the periodic Poisson equation. In practice we run all these cases using a 1D2V implementation of the above methods. When the initial distribution is only 1D1V we sample the particles following a Maxwellian in  $v_2$  with thermal velocity  $\sigma_2 = 1$ .

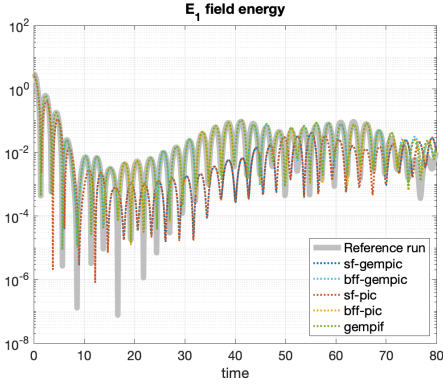
## 5.2 Qualitative energy behaviors

In order to compare the qualitative response of the different schemes, we first plot the relevant energy curves for the above test-cases using rather coarse numerical parameters such as  $K$ ,  $M$  and  $\kappa$ , but a number of particles  $N$  high enough to match the reference damping or growth rates.

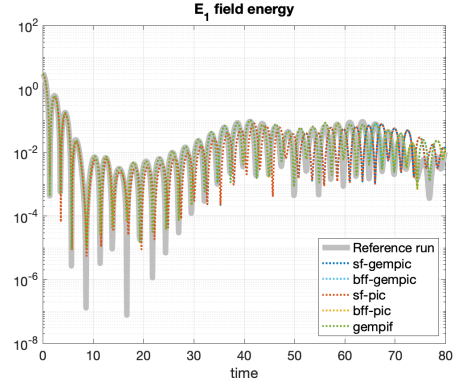
In Figure 1 and 2 we plot the energy curves for the above test cases, using  $K = 3$  Fourier modes, splines of degree  $\kappa = 3$  and DFT grids with  $M = 8$  (left) or  $M = 16$  points (right). For the strong (top) and weak (bottom) Landau damping test-cases in Figure 1 we use  $N = 5 \cdot 10^4$  and  $N = 10^5$  particles, respectively. For the Weibel (top), two-stream (center) and bump-on-tail instabilities in Figure 2 we use  $N = 10^4$ ,  $N = 5 \cdot 10^4$  and  $N = 10^5$  particles, respectively. The gray curves show reference runs, obtained using the GEMPIF scheme with  $5 \cdot 10^6$  particles and  $K = 15$  Fourier modes. In all these runs, the time scheme is given by a fourth-order (Suzuki-Yoshida) composition method (74) with a time step of  $\Delta t = 0.1$ .

Our first observation is that the qualitative energy behaviors of the different simulations essentially depends on whether the method is back-filtered or not. Indeed we see that for each test-case the energy curves of the BFF-GEMPIC and BFF-PIC methods are perfectly on top of that of the gridless GEMPIF method, and they match very well the reference energy curve. Moreover, their numerical damping and growth rates (not reported here) agree with the reference ones, either given by dispersion relations from linear theory, or available in reference results from the literature, as in the strong Landau damping. (For the bump-on-tail instability the agreement of the numerical growth rates is weaker, but this test-case is known to be more demanding in terms of particles.) In contrast, the methods SF-GEMPIC and SF-PIC involving a regular smoothed-Fourier coupling are also on top of each other, but in many cases they do not match the reference curve. This is most visible with the coarsest grid or in the bump-on-tail test-case, where the growth rates are clearly wrong. With the finer grid (corresponding to an oversampling factor of  $\mu = 16/7 \approx 2$ ), the results on the right panels show an improvement of the energy accuracy, but not as good as with back-filtering. Thus, these simulations show a clear benefit of back-filtered Fourier-PIC schemes in the qualitative energy behavior of low-resolution methods.

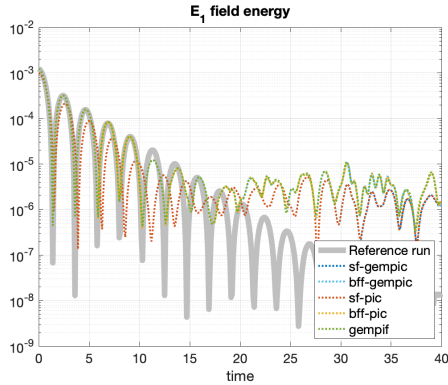
In order to see the effect of using high order splines, we plot in Figure 3 the energy curves obtained using splines of degree  $\kappa = 5$  for some of the above test cases. For the two filtered methods, this has no visible effect: they are still on top of the gridless method (which involves no splines). For the two unfiltered methods this actually degrades the results, as the energy curves are more distant from the reference one than with  $\kappa = 3$ .



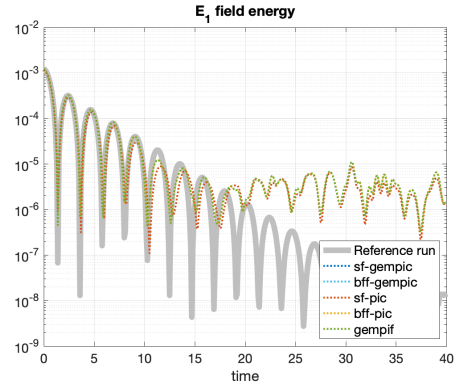
(a) strong damping with an  $M = 8$  grid



(b) strong damping with an  $M = 16$  grid

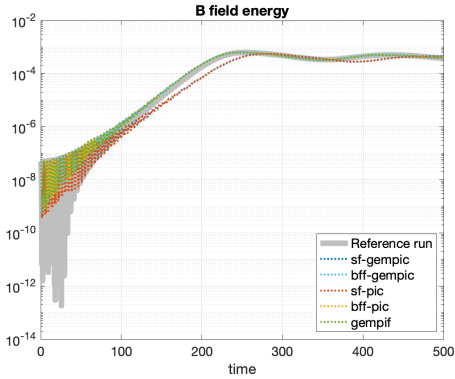


(c) weak damping with an  $M = 8$  grid

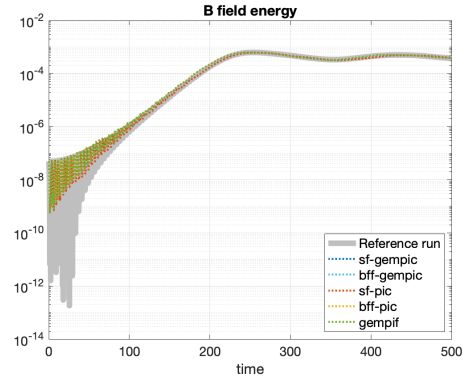


(d) weak damping with an  $M = 16$  grid

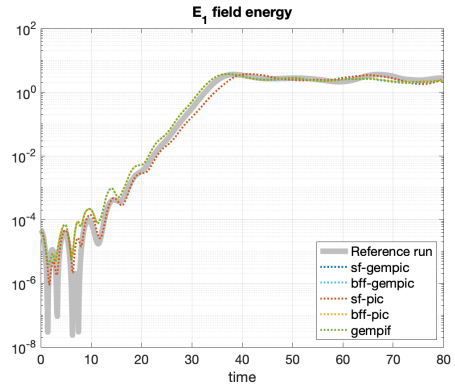
Figure 1: Landau damping test-cases:  $E_1$  field energy curves, using  $K = 3$  Fourier modes,  $N = 5 \cdot 10^4$  particles for the strong damping (top) and  $N = 10^5$  for the weak damping (bottom). Gridded (GEMPIC and PIC) methods use B-spline shapes of degree  $\kappa = 3$  and DFT grids with  $M = 8$  (left) or  $M = 16$  points (right).



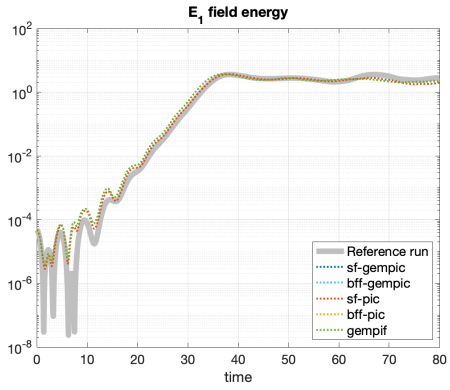
(a) Weibel instability with an  $M = 8$  grid



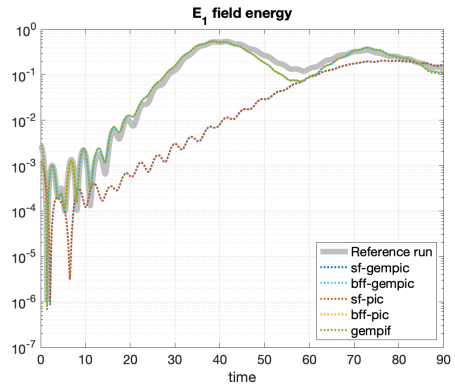
(b) Weibel instability with an  $M = 16$  grid



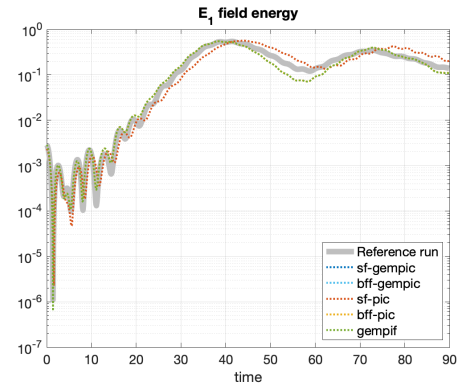
(c) two stream instability with an  $M = 8$  grid



(d) two stream instability with an  $M = 16$  grid

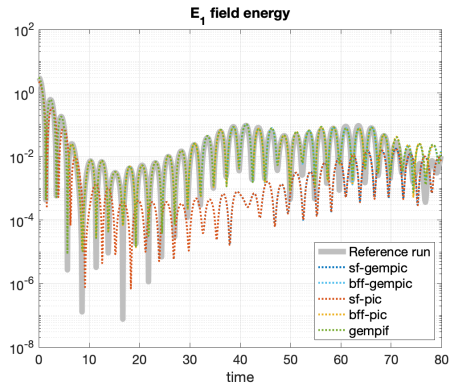


(e) bump-on-tail instability with an  $M = 8$  grid

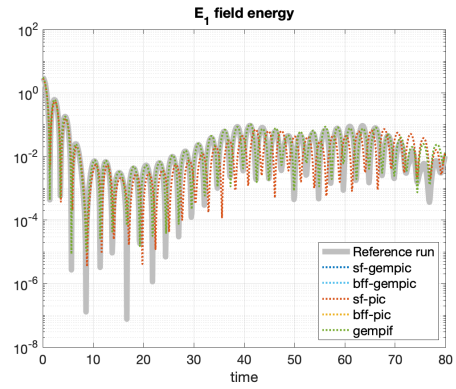


(f) bump-on-tail instability with an  $M = 16$  grid

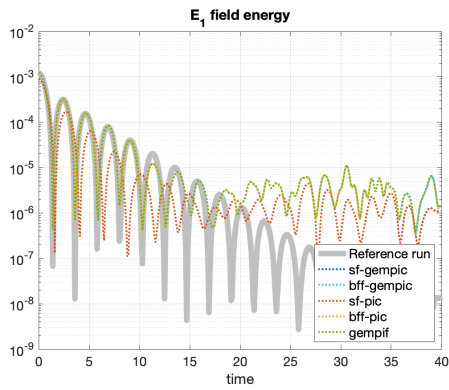
Figure 2: Energy behavior for instability test-cases:  $B_3$  field energy for the Weibel instability (top) using  $N = 10^4$  particles, and  $E_1$  field energy for the two-stream (center) and bump-on-tail instabilities (bottom), using  $N = 5 \cdot 10^4$  and  $N = 10^5$  particles, respectively. All runs use  $K = 3$  Fourier modes, and gridded (GEMPIC and PIC) methods use B-spline shapes of degree  $\kappa = 3$  and DFT grids with  $M = 8$  (left) or  $M = 16$  points (right).



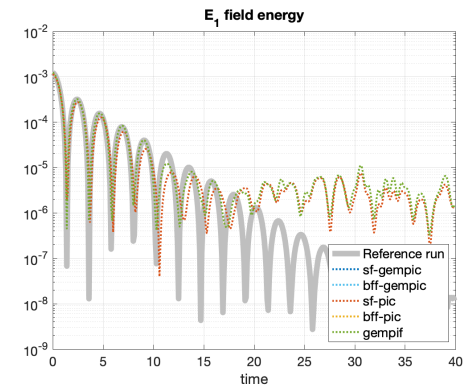
(a) strong damping with an  $M = 8$  grid



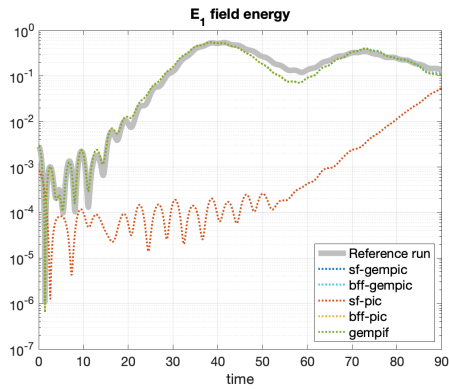
(b) strong damping with an  $M = 16$  grid



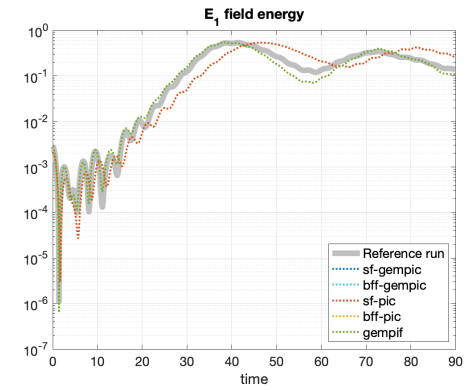
(c) weak damping with an  $M = 8$  grid



(d) weak damping with an  $M = 16$  grid



(e) bump-on-tail instability with an  $M = 8$  grid



(f) bump-on-tail instability with an  $M = 16$  grid

Figure 3: Landau damping and bump-on-tail instability test-cases, using the same parameters as in Figures 1 and 2 and B-spline shapes of degree  $\kappa = 5$ .

### 5.3 Long-time conservation properties

In order to assess the long-time conservation properties of the different methods, we show in Figure 4 several errors for the Weibel instability test-case on a time range ten times longer than above. The plotted errors are in energy conservation,

$$\text{Err}_{\mathcal{H}}^n = \frac{|\mathcal{H}^n - \mathcal{H}^0|}{\mathcal{H}^0} \quad \text{with} \quad \mathcal{H}^n = \frac{1}{2} \sum_{p=1}^N m_p |\mathbf{V}_p^n|^2 + \frac{1}{2} \int_{[0,L]} \left( |\mathbf{E}_K^n(x)|^2 + |\mathbf{B}_K^n(x)|^2 \right) dx \quad (90)$$

momentum conservation,

$$\text{Err}_{\mathcal{P}}^n = \frac{\|\mathcal{P}^n - \mathcal{P}^0\|_1}{\|\mathcal{P}^0\|_1} \quad \text{with} \quad \mathcal{P}^n = \sum_{p=1}^N m_p \mathbf{V}_p^n + \int_{[0,L]} \mathbf{E}_K^n(x) \times \mathbf{B}_K^n(x) dx \quad (91)$$

and Gauss law

$$\text{Err}_G^n = \int_{[0,L]} \left| \left( \text{div} \mathbf{E}_K^n - \sum_{p=1}^N q_p \Pi^3 S_{\mathbf{X}_p^n} \right) (x) \right|^2 dx. \quad (92)$$

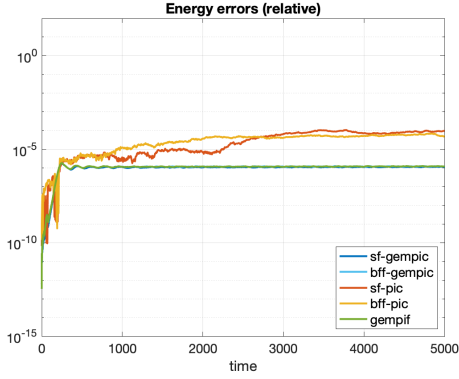
For each method we use the same numerical parameters as in Figure 2, and low-resolution runs with spline shapes of degree  $\kappa = 3$  and  $\kappa = 7$ .

For the energy conservation we observe overall a good behavior for all the methods. Here the main observation is that a clear separation is visible between the three geometric methods and the two non-geometric ones. While the former show a very good stability of the energy conservation over these long-time ranges, the latter sometimes display sensible growth in the energy error, characteristic of a less stable behavior. Another interesting difference is that when the DFT grid is refined (right plots), the energy errors made by the non-geometric methods get reduced, while those of the geometric methods hardly change. This behavior is consistent with the backward error analysis which states that Hamiltonian splitting time integrators of order  $q$  preserve exactly a modified energy which approximates the exact one with the same order.

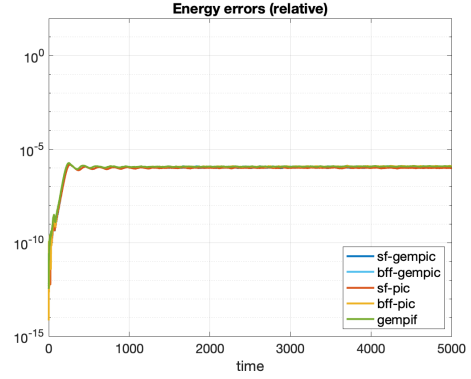
As for the momentum conservation, the first observation is that the curves confirm the exact conservation of the GEMPIF method and the two non-geometric schemes (SF-PIC and BFF-PIC). For the Fourier-GEMPIC methods the conservation is only approximate, however we observe a very good stability over these long-time simulations. We also observe that the accuracy to which the momentum is preserved is improved by refining grid or increasing the spline order.

Finally the Gauss error curves confirm the exact charge conserving property of all methods.

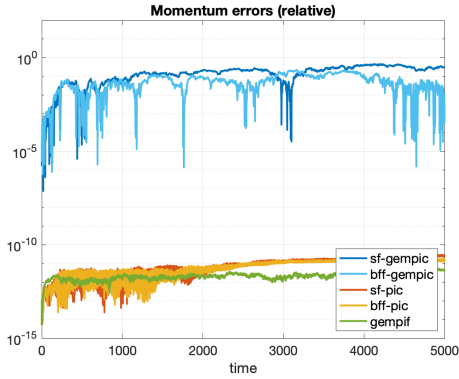




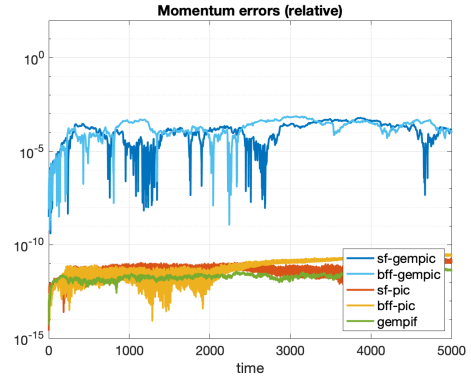
(a) Energy errors with shapes of degree  $\kappa = 3$



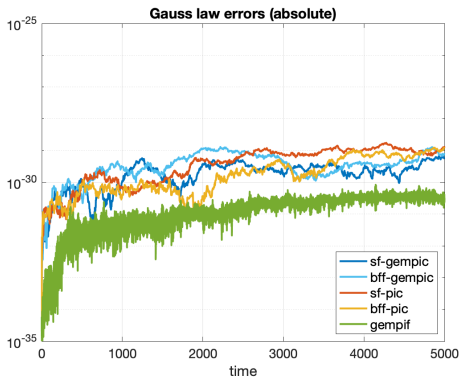
(b) Energy errors with shapes of degree  $\kappa = 7$



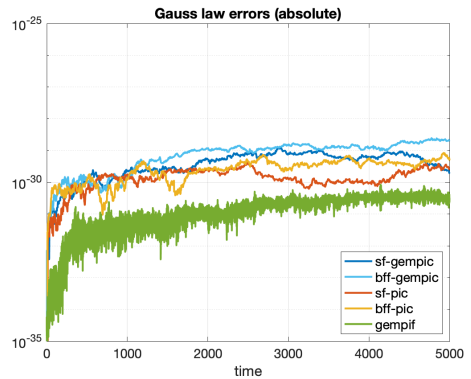
(c) Momentum errors with shapes of degree  $\kappa = 3$



(d) Momentum errors with shapes of degree  $\kappa = 7$



(e) Gauss law errors with shapes of degree  $\kappa = 3$



(f) Gauss law errors with shapes of degree  $\kappa = 7$

Figure 4: Long-time conservation properties. Energy conservation errors (top), momentum conservation errors (middle) and Gauss law errors (bottom) are shown for Weibel instability runs using  $N = 10^4$  particles and  $K = 3$  Fourier modes. Gridded (Fourier-Gempic and Fourier-PIC) methods use a DFT grid with  $M = 16$  points corresponding to an oversampling parameter of  $\mu = \frac{M}{2K+1} \approx 2.3$  and B-spline shapes of degree  $\kappa = 3$  (left) or  $\kappa = 7$  (right). Similar curves have been observed for higher resolution runs with analogous oversampling parameter, such as  $K = 13$  and  $M = 64$ . Compared to the runs in Fig. 2, the simulation range is ten times longer.

## 5.4 Convergence studies

We finally study how the conservation of energy and momentum is improved by refining the numerical parameters.

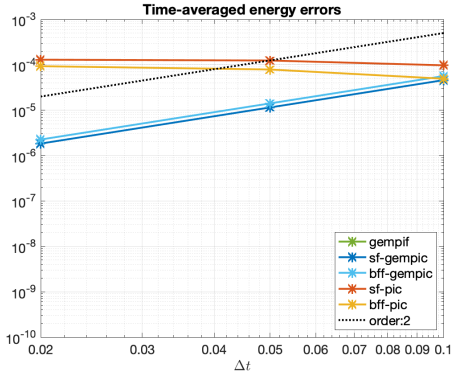
In Figure 5 and 6 we plot the time-averaged energy errors  $\frac{1}{N_t} \sum_{n=0}^{N_t-1} \text{Err}_{\mathcal{H}}^n$ , for the five methods (using the same color key as above) as a function of the time step, for various DFT grids and spline degrees. Results shown in Figure 5 are obtained with the second order Strang scheme (73), while those in Figure 6 correspond to the fourth-order Suzuki-Yoshida scheme (74). For an easier comparison, both figures use the same scale.

For the non-geometric methods we observe an improvement in the energy errors when the time step decreases, but the convergence is limited by the resolution of the grid and the degree of the splines. This artifact is not present with the geometric methods, where the convergence of the energy errors holds almost independently of the grid resolution and spline degree. This confirms the behavior already observed in the long-time runs, see Figure 4. It is also in strong agreement with the backward error analysis, which predicts a convergence of the energy errors of the same order as the time scheme. Here the runs correspond to the Weibel instability with a moderate time range ( $T = 500$ ), but results obtained with other test cases have showed similar behavior.

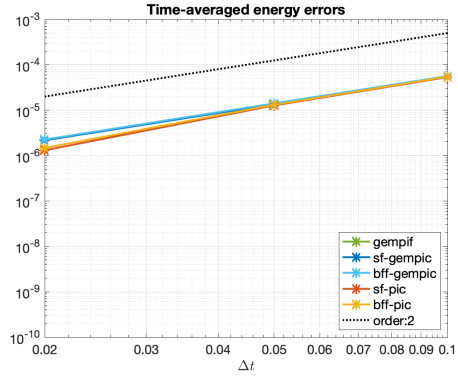
In Figure 7 we plot the time-averaged momentum errors  $\frac{1}{N_t} \sum_{n=0}^{N_t-1} \text{Err}_{\mathcal{P}}^n$ , for the five methods (again with the same color key), as a function of the ratio  $2K/M \approx 1/\mu$ , for various spline degrees. For the GEMPIF and Fourier-PIC methods the error is close to machine accuracy, since the methods are exactly momentum conserving. For the Fourier-GEMPIC methods we observe that in every case they converge to 0, with a rate close to  $\mathcal{O}(K/M)^{\kappa+1}$ . Here the test-case is again the Weibel instability with  $K = 3$  modes as in Section 5.2, but the same convergence behavior was observed with other test-cases and a higher number of Fourier modes.

## 6 Acknowledgements

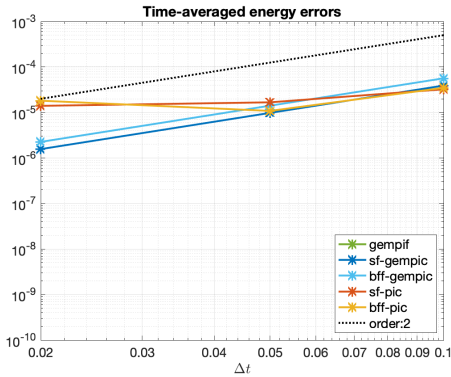
This work has been carried out within the framework of the EUROfusion Consortium and has received funding from the Euratom research and training programme 2014-2018 and 2019-2020 under grant agreement No 633053. The views and opinions expressed herein do not necessarily reflect those of the European Commission.



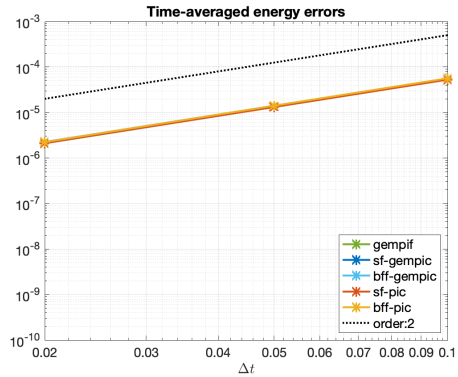
(a)  $M = 8$  and  $\kappa = 3$



(b)  $M = 16$  and  $\kappa = 3$

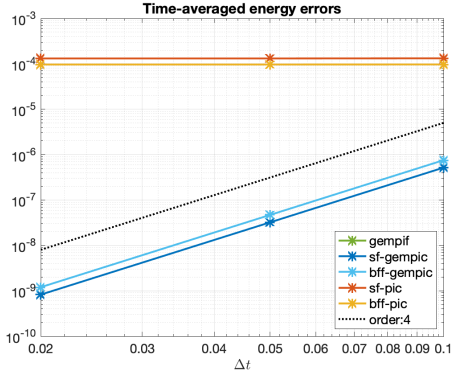


(c)  $M = 8$  and  $\kappa = 5$

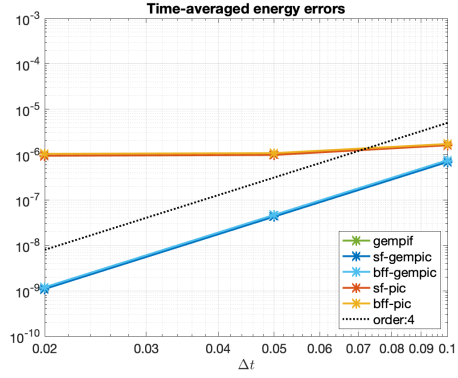


(d)  $M = 16$  and  $\kappa = 5$

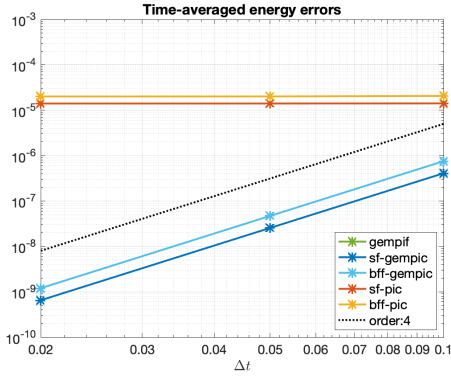
Figure 5: Energy error convergence: time-averaged energy conservation errors as a function of the time step  $\Delta t$ , for a Weibel instability test-case with  $K = 3$  Fourier modes,  $N = 5 \cdot 10^4$  particles and various grids and spline degrees, as indicated. Results reported here use a second-order (Strang) time scheme.



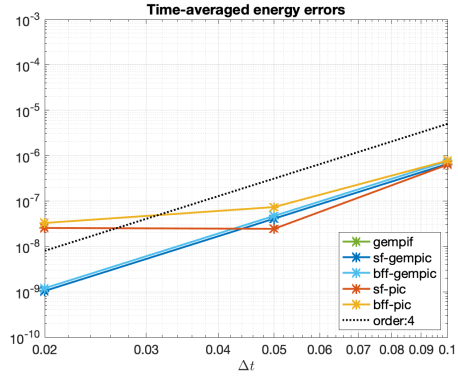
(a)  $M = 8$  and  $\kappa = 3$



(b)  $M = 16$  and  $\kappa = 3$

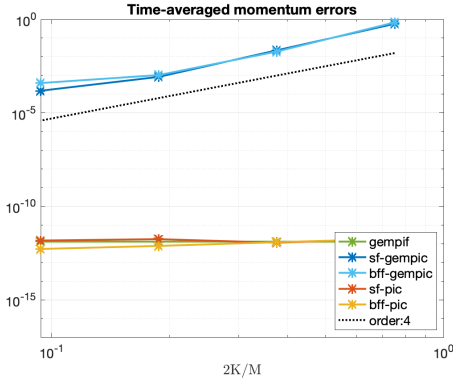


(c)  $M = 8$  and  $\kappa = 5$

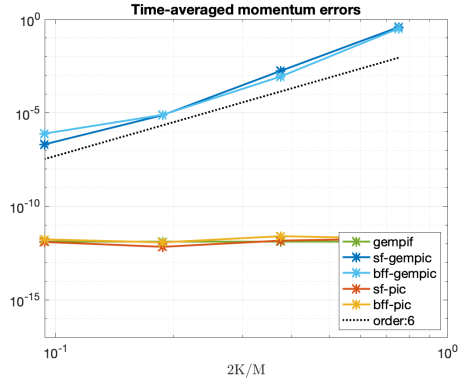


(d)  $M = 16$  and  $\kappa = 5$

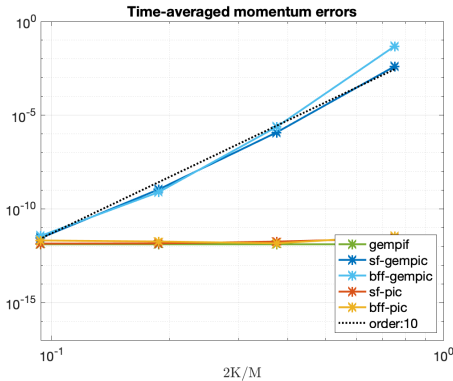
Figure 6: Energy error convergence curves, using the same parameters as in Figure 5, and a fourth-order (Suzuki-Yoshida) time scheme.



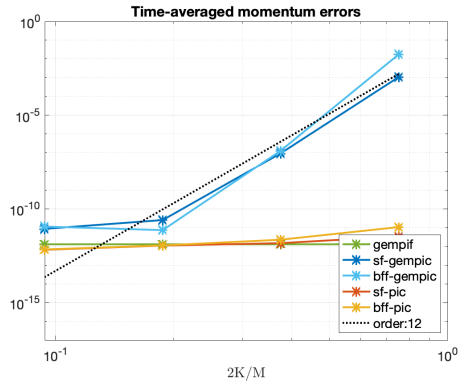
(a) Spline degree  $\kappa = 3$



(b) Spline degree  $\kappa = 5$



(c) Spline degree  $\kappa = 9$



(d) Spline degree  $\kappa = 11$

Figure 7: Momentum error convergence: time-averaged momentum conservation errors as a function of the ratio  $2K/M$ , using the Weibel instability test-case with  $K = 3$  Fourier modes,  $N = 5 \cdot 10^4$  particles and spline degrees as indicated. Results reported here use a fourth-order (Suzuki-Yoshida) time scheme.

## References

- [1] Jakob Ameres. *Stochastic and Spectral Particle Methods for Plasma Physics*. Dissertation, Technische Universität München, München, 2018.
- [2] Douglas N. Arnold, Richard S. Falk, and Ragnar Winther. Finite Element Exterior Calculus: from Hodge theory to numerical stability. *Bulletin of the American Mathematical Society*, 47:281–354, 2010. doi: 10.1090/S0273-0979-10-01278-4.
- [3] C K Birdsall and A.B. Langdon. *Plasma physics via computer simulation*. Adam Hilger, IOP Publishing, 1991.
- [4] Charles K. Birdsall and Neil Maron. Plasma self-heating and saturation due to numerical instabilities. *J. Comput. Physics*, 36(1):1–19, June 1980.
- [5] R B Blackman and J W Tukey. *The Measurement of Power Spectra*. Dover, 1958.
- [6] Alain Bossavit. *Computational electromagnetism: variational formulations, complementarity, edge elements*. Academic Press, 1998.
- [7] Annalisa Buffa, Giancarlo Sangalli, and Rafael Vázquez. Isogeometric analysis in electromagnetics: B-splines approximation. *Computer Methods in Applied Mechanics and Engineering*, 199(17):1143–1152, 2010. doi: 10.1016/j.cma.2009.12.002.
- [8] Martin Campos Pinto and Eric Sonnendrücker. Compatible Maxwell solvers with particles I: conforming and non-conforming 2d schemes with a strong Ampere law. *The SMAI journal of computational mathematics*, 3:53–89, 2017. doi: 10.5802/smai-jcm.20. URL [smi-jcm.centre-mersenne.org/item/SMAI-JCM\\_2017\\_\\_3\\_\\_53\\_0/](https://smi-jcm.centre-mersenne.org/item/SMAI-JCM_2017__3__53_0/).
- [9] Martin Campos Pinto, Katharina Kormann, and Eric Sonnendrücker. Variational framework for structure-preserving electromagnetic Particle-In-Cell methods. *arXiv preprint arXiv:2101.09247*, 2021.
- [10] Nicolas Crouseilles, Lukas Einkemmer, and Erwan Faou. Hamiltonian splitting for the Vlasov–Maxwell equations. *Journal of Computational Physics*, 283:224–240, 2015. doi: 10.1016/j.jcp.2014.11.029.
- [11] Viktor K Decyk. Description of Spectral Particle-in-Cell Codes from the UPIC Framework. *Presentation at ISSS-10*, 2011. URL <https://picksc.idre.ucla.edu/wp-content/uploads/2015/05/UPICModels.pdf>.
- [12] T Zh Esirkepov. Exact charge conservation scheme for particle-in-cell simulation with an arbitrary form-factor. *Computer Physics Communications*, 135(2):144–153, 2001.
- [13] Evstati G. Evstatiev and Bradley A. Shadwick. Variational formulation of particle algorithms for kinetic plasma simulations. *Journal of Computational Physics*, 245:376–398, 2013. doi: 10.1016/j.jcp.2013.03.006.
- [14] Claude Gasquet and Patrick Witomski. *Fourier Analysis and Applications*, volume 30 of *Texts in Applied Mathematics*. Springer New York, New York, NY, 1999.
- [15] Brendan B Godfrey. Numerical Cherenkov instabilities in electromagnetic particle codes. *Journal of Computational Physics*, 15(4):504–521, August 1974.

- [16] Brendan B Godfrey, Jean-Luc Vay, and Irving Haber. Numerical stability analysis of the pseudo-spectral analytical time-domain PIC algorithm. *Journal of Computational Physics*, 258:689–704, February 2014.
- [17] Ernst Hairer, Christian Lubich, and Gerhard Wanner. *Geometric Numerical Integration*. Springer, 2006.
- [18] R Hatzky, R Kleiber, A Könies, A Mishchenko, M Borchardt, A Bottino, and E. Sonnendrücker. Reduction of the statistical error in electromagnetic gyrokinetic particle-in-cell simulations. *Journal of Plasma Physics*, 85(1):905850112, 2019. doi: 10.1017/S0022377819000096.
- [19] Yang He, Hong Qin, Yajuan Sun, Jianyuan Xiao, Ruili Zhang, and Jian Liu. Hamiltonian integration methods for Vlasov–Maxwell equations. *Physics of Plasmas*, 22:124503, 2015. doi: 10.1063/1.4938034.
- [20] Ralf Hiptmair. Finite elements in computational electromagnetism. *Acta Numerica*, 11: 237–339, 2002.
- [21] R.W. Hockney and J.W. Eastwood. *Computer simulation using particles*. Taylor & Francis, Inc, Bristol, PA, USA, 1988.
- [22] C-K Huang, Yong Zeng, Ying Wang, Michael D Meyers, Sunghwan Yi, and Brian J Albright. Finite grid instability and spectral fidelity of the electrostatic particle-in-cell algorithm. *Computer Physics Communications*, 207:123–135, 2016.
- [23] Michael Kraus, Katharina Kormann, Philip J. Morrison, and Eric Sonnendrücker. GEM-PIC: Geometric electromagnetic particle-in-cell methods. *Journal of Plasma Physics*, 83 (4), 2017.
- [24] A Bruce Langdon. Effects of the spatial grid in simulation plasmas. *Journal of Computational Physics*, 6(2):247–267, October 1970.
- [25] A Bruce Langdon. Kinetic theory for fluctuations and noise in computer simulation of plasma. *Physics of Fluids*, 22(1):163–10, 1979.
- [26] A Bruce Langdon and Charles K. Birdsall. Theory of Plasma Simulation Using Finite-Size Particles. *Physics of Fluids*, 13(8):2115–2122, August 1970.
- [27] Robert I. McLachlan and G. Reinout W. Quispel. Splitting methods. *Acta Numerica*, 11: 341–434, 2002. doi: 10.1017/S0962492902000053.
- [28] B F McMillan, S Jolliet, A Bottino, P Angelino, T M Tran, and L Villard. Rapid Fourier space solution of linear partial integro-differential equations in toroidal magnetic confinement geometries. *Computer Physics Communications*, 181(4):715 – 719, 04 2010. doi: 10.1016/j.cpc.2009.12.001.
- [29] Matthew S Mitchell, Matthew T Miecnikowski, Gregory Beylkin, and Scott E Parker. Efficient Fourier Basis Particle Simulation. *Journal of Computational Physics*, pages 837–847, August 2019.

- [30] N Ohana, A Jocksch, E Lanti, TM Tran, S Brunner, C Gheller, F Hariri, and L Villard. Towards the optimization of a gyrokinetic Particle-In-Cell (PIC) code on large-scale hybrid architectures. In *Journal of Physics: Conference Series*, volume 775, page 012010. IOP Publishing, 2016.
- [31] Okuda, Hideo. Nonphysical noises and instabilities in plasma simulation due to a spatial grid. *J. Comput. Physics*, 10(3):475–486, December 1972.
- [32] Gerlind Plonka, Daniel Potts, Gabriele Steidl, and Manfred Tasche. Fast Fourier Transforms for Nonequispaced Data. In *Numerical Fourier Analysis*, pages 377–419. Birkhäuser, Cham, Cham, 2018.
- [33] Bradley A. Shadwick, Alexander B. Stamm, and Evstati G. Evstatiev. Variational formulation of macro-particle plasma simulation algorithms. *Physics of Plasmas*, 21(5):055708, 2014. doi: 10.1063/1.4874338.
- [34] Gabriele Steidl. A note on fast Fourier transforms for nonequispaced grids. *Advances in Computational Mathematics*, 9(3-4):337–352, 1998.
- [35] Jean-Luc Vay, Irving Haber, and Brendan B Godfrey. A domain decomposition method for pseudo-spectral electromagnetic simulations of plasmas. *Journal of Computational Physics*, 243:260–268, June 2013.
- [36] Jr H D Victory and Edward J Allen. The Convergence Theory of Particle-In-Cell Methods for Multidimensional Vlasov–Poisson Systems. *SIAM Journal on Numerical Analysis*, 28(5):1207 – 1241, 1991. doi: 10.1137/0728065. URL <http://epubs.siam.org/doi/abs/10.1137/0728065>.
- [37] G Vlad, S Briguglio, G Fogaccia, and B Di Martino. Gridless finite-size-particle plasma simulation. *Computer physics communications*, 134(1):58–77, 2001.
- [38] Stephen D Webb. A spectral canonical electrostatic algorithm. *Plasma Physics and Controlled Fusion*, 58(3):034007, 2016.
- [39] Erich S. Weibel. Spontaneously growing transverse waves in a plasma due to an anisotropic velocity distribution. *Physical Review Letters*, 2:83–84, 1959. doi: 10.1103/PhysRevLett.2.83.
- [40] Xinlu Xu, Peicheng Yu, Samual F Martins, Frank S Tsung, Viktor K Decyk, Jorge Vieira, Ricardo A Fonseca, Wei Lu, Luis O Silva, and Warren B Mori. Numerical instability due to relativistic plasma drift in EM-PIC simulations. *Computer Physics Communications*, 184(11):2503–2514, November 2013.